PDZ-directed substrate recruitment is the primary determinant of specific 4E-BP1 dephosphorylation by PP1-Neurabin

Roman O Fedoryshchak[1], Karim El-Bouri[2^], Dhira Joshi[3], Stephane Mouilleron[2], Richard Treisman[1,*]

1 Signalling and transcription Laboratory,

2 Structural Biology STP,

3 Chemical Biology STP,

Francis Crick Institute, 1 Midland Road, London NW1 1AT, UK

Current address:

^ Protein Biogenesis Laboratory, Francis Crick Institute, 1 Midland Road, London NW1 1AT, UK

* Corresponding Author: Richard.Treisman@crick.ac.uk

ORCID ID: ROF: 0000-0003-1865-8372; KE-B, 0000-0002-4542-0856; DJ, 0000-0001-8660-2528; SM, 0000-0001-7977-6298; RT: 0000-0002-9658-0067.

Running title: Substrate-specificity determinants in Neurabin/Spinophilin

Keywords: PP1, Phactr, Neurabin, Spinophilin, PNUTS, PPP1R15A, PIP, mTORC1

ABSTRACT

Protein Phosphatase 1 (PP1) relies on association with PP1-interacting proteins (PIPs) to generate substrate-specific PIP/PP1 holoenzymes, but the lack of well-defined substrates has hindered elucidation of the mechanisms involved. We previously demonstrated that the Phactr1 PIP confers sequence specificity on the Phactr1/PP1 holoenzyme by remodelling the PP1 hydrophobic substrate groove. Phactr1 defines a group of “RVxF-ΦΦ-R-W” PIPs that all interact with PP1 in a similar fashion. Here we use a PP1-PIP fusion approach to address sequence specificity and identify substrates of the RVxF-ΦΦ-R-W family PIPs. We show that the four Phactr proteins confer identical sequence specificities on their holoenzymes. We identify the 4E-BP and p70 S6K translational regulators as substrates for the Neurabin/Spinophilin PIPs, implicated in neuronal plasticity, pointing to a role for their holoenzymes in mTORC1-dependent translational control. Biochemical and structural experiments show that in contrast to the Phactrs, substrate recruitment and catalytic efficiency of the PP1-Neurabin and PP1-Spinophilin fusions is primarily determined by substrate interaction with the PDZ domain adjoining their RVxF-ΦΦ-R-W motifs, rather than by recognition of the remodelled PP1 hydrophobic groove. Thus, even PIPs that interact with PP1 in a similar manner use different mechanisms to ensure substrate selectivity.

INTRODUCTION

Phosphoprotein Phosphatase 1 (PP1) is a member of the PPP superfamily of protein phosphatases, responsible for most cellular serine/threonine dephosphorylation (Bollen et al, 2010; Brautigan and Shenolikar, 2018). The three PP1 isoforms possess a central metal-binding active centre from which radiate three putative substrate-binding grooves (Egloff et al, 1995; Goldberg et al, 1995), but have little intrinsic sequence specificity (Hoermann et al, 2020). Instead, PP1 substrate specificity and activity is controlled by over 200 PP1 interacting proteins (PIPs), which use a number of short linear motifs (SLIMs) to dock with distinct regions of the PP1 surface, including the substrate-binding grooves (Cohen, 2002; Bollen et al., 2010; Casamayor and Arino, 2020). PIPs can target PP1 to specific subcellular locations, and can control substrate specificity through autonomous substrate-binding domains, occupation or extension of the substrate grooves, or modification of PP1 surface electrostatics (for references see Bollen et al., 2010; Fedoryshchak et al, 2020). Only a few PIP-PP1-substrate interactions are understood in molecular detail, however, and the question of whether PIP interaction imposes sequence specificity on PP1, as opposed to simply bringing enzyme and substrate into close apposition, has remained largely unexplored.

The Phactr family of actin-regulated PP1 cofactors are the only PIPs known to directly impose substrate sequence-specificity at the dephosphorylation site itself (Fedoryshchak et al., 2020). Like many PIPs, they interact with PP1 using the previously defined “RVxF”, “ΦΦ”, and “R” motifs (Choy et al, 2014). Structural alignment showed that the Phactrs belong to a subset of RVxF-ΦΦ-R PIPs whose shared trajectory across the PP1 surface continues to the edge of the hydrophobic groove, making an additional PP1 contact through an additional motif that we termed

the “W” SLIM (Ragusa et al, 2010; Choy et al., 2014; Chen et al, 2015; Fedoryshchak et al., 2020; Yan et al, 2021) (Figure 1A, Figure 1-S1A). These “RVxF-ΦΦ-R-W string” PIPs include Neurabin/Spinophilin (PPP1R9A/B), which play important roles in PP1-dependent regulation of neuronal plasticity (Allen et al, 1997; Burnett, 1998 #87, reviewed by Sarrouilhe et al, 2006; Foley et al, 2021); PNUTS (PPP1R10), which regulates PolII and chromatin dynamics (Lee et al, 2010; Cortazar et al, 2019); and PPP1R15A/B, which mediate translational regulation through control of eIF2α dephosphorylation (Novoa et al, 2001; Chen et al., 2015; Yan et al., 2021)(Figure 1A). In the Phactr1-PP1 holoenzyme, Phactr1 sequences C-terminal to the RVxF-ΦΦ-R-W string interact with the PP1 hydrophobic groove to form a composite hydrophobic pocket, topped by a basic rim. This imposes strong sequence selectivity on substrates, favouring hydrophobic residues at positions +4/+5 relative to the phosphorylated residue, within an acidic context (consensus pS/T-$x_{(2-3)}$-Φ-L, the “LLD motif”). Strikingly, this specificity is maintained in a PP1-Phactr1 fusion protein comprising PP1(1-304) linked to Phactr1 sequences from residue 526, just C-terminal to its RVxF motif (Fedoryshchak et al., 2020).

Neurabin and Spinophilin remodel the PP1 hydrophobic groove differently from Phactr1, generating a structurally distinct surface on the holoenzyme, and it is likely that the other RVxF-ΦΦ-R-W PIPs do so as well (Ragusa et al., 2010; Fedoryshchak et al., 2020) (see Figure 1A, Figure 1-S2). Whether and how these diverse surfaces might play a role in the substrate specificity of these PIP/PP1 holoenzymes has remained unclear, largely because little is known about their substrates. Here we investigate determinants of substrate specificity in the other RVxF-ΦΦ-R-W PIPs, focussing on Neurabin/Spinophilin, which also contain a PDZ domain previously suggested to be involved in substrate recruitment (Burnett et al,

1998; Kelker et al, 2007). We use the PP1-PIP fusion approach to show that the four Phactr1 holoenzymes have indistinguishable substrate specificities, and to identify novel candidate substrates for the other RVxF-ΦΦ-R-W PIP/PP1 complexes. We use 4E-BP1, a new Neurabin/PP1 substrate, to show that unlike the Phactr1/PP1 holoenzyme, substrate specificity of Neurabin/PP1 is largely determined by interaction with the Neurabin PDZ domain rather than the primary sequences of the dephosphorylation site itself.

RESULTS

PP1-PIP fusion proteins

The PP1 C-terminal sequences closely approach the Phactr1 RVxF-ΦΦ-R-W string in the vicinity of the ΦΦ motif, which allowed the construction of a single chain PP1α -PIP fusion derivative comprising PP1α(7-304) linked to Phactr1 sequences from a point just C-terminal to its RVxF motif (Figure 1A, Figure 1-S1A, S2A). The remodelled hydrophobic groove of this fusion is structurally identical to that of the Phactr/PP1 holoenzyme, and it retains similar activity and specificity(Fedoryshchak et al., 2020). Guided by the structures of the other RVxF-ΦΦ-R-W PIPs, we generated analogous fusions of N-terminally Flag-tagged PP1 with fragments of Neurabin and Spinophilin (Figure 1-S2B, S2C) (PPP1R9A/B,Ragusa et al., 2010), PNUTS (Figure 1-S2C) (PPP1R10, Choy et al., 2014), and PPP1R15A and PPP1R15B (Figure 1-S2E, 1-S2F)(Chen et al., 2015; Yan et al., 2021), comprising the PP1-interacting sequences and any known protein interaction domains immediately C-terminal to them. We also constructed fusions with each the four Phactr proteins to explore any variation in their sequence specificities (Figure 1A; Figure 1-S1A, 1-S2A).

Each fusion protein was stably expressed in 293 Flp-In T-Rex cells using a tetracycline-inducible vector (Ward et al, 2011). Tetracycline titration of PP1-Phactr1 cells induced increasing expression of the fusion protein, leading to corresponding dephosphorylation of its substrates IRSp53 pS455 and Afadin pS1275 (Fedoryshchak et al., 2020) (Figure 1B). Afadin pS1275 was dephosphorylated by all four PP1-Phactr fusions, but not by the other PP1-PIP fusions (Figure 1C). Similar results were observed with exogenously expressed wildtype IRSp53. In this setting, alanine substitution of IRSp53 L460, which contacts the novel Phactr1/PP1

hydrophobic pocket and impairs dephosphorylation by the intact Phactr1/PP1 holoenzyme (Fedoryshchak et al., 2020), also impaired dephosphorylation by all the PP1-Phactr fusions, indicating that they recognise phosphorylated IRSp53 in a similar way (Figure 1-S1B).

Proteomic analysis of PP1-fusion specificity

To investigate the substrate specificities of the fusion proteins, we performed Tandem-Mass-Tag (TMT) phosphoproteomics. Fractionated peptides were measured in both MS2 and MS3 modes for maximal identification and quantification (Figure 2A). Phosphorylation site abundances within triplicate samples from the same cell line were comparable between replicates (Figure 2B). First, we identified phosphorylation sites significantly depleted by expression of PP1α(7-304) alone compared with vector only, using Perseus software and a t-test with a 1% permutation-based false-discovery rate cutoff (Tyanova et al, 2016). In agreement with previous results (Hoermann et al., 2020), PP1 exhibited little sequence specificity, other than a preference for positively charged residues in positions -3, -1 and +3 to the dephosphorylation site (Figure 2-S1A, 2-S1B).

We then compared the specificities of the four PP1-Phactr fusion proteins. Expression of PP1-Phactr1 revealed numerous phosphorylation sites that were specifically depleted compared with cells expressing PP1α alone (Figure 2C). This population contained many of the Phactr1/PP1 holoenzyme substrates previously identified in neurons or NIH3T3 fibroblasts, including IRSp53 pS455 and Afadin pS1275 (Figure 2C)(Fedoryshchak et al., 2020). Of the 28 top Phactr1/PP1 hits previously identified in NIH3T3 cells, 18 were detectable in the 293 system, of which 13 also registered as PP1-Phactr1 hits (Figure 2-S1C). The putative PP1-Phactr1

substrates were also substantially enriched in the Phactr1/PP1 consensus dephosphorylation motif S/T-$x_{2,3}$-Φ-L (Figure 2D). The profiles of PP1-Phactr2, PP1-Phactr3, and PP1-Phactr4 cells were substantially similar to that of PP1-Phactr1 (Figure 2-S1D,E,F), exhibiting good overall correlations both between total phosphorylation site profiles (Figure 2B), and significant enrichment for both the S/T-$x_{2,3}$-Φ-L motif and specific Phactr1/PP1 substrates (Figure 2D; Figure 2-S1C); over 60% of the depleted phosphorylation sites were in common between all four fusions (Figure 2E). These data show that the PP1-Phactr fusions recapitulate the specificity of the Phactr1/PP1 holoenzyme.

We next used the proteomics approach to investigate protein dephosphorylation by the PP1-R15A/B and PP1-PNUTS fusion proteins, comparing each fusion to all the others (other than its paralog) or PP1α alone (Figure 2B). PPP1R15A has a well-validated substrate, eIF2α pS51 (Novoa et al., 2001), whose effective dephosphorylation requires additional recruitment of G-actin to the PPP1R15A/PP1 complex (Chen et al., 2015; Yan et al., 2021). The eIF2α pS51 phosphorylation site was not detected in the dataset, however, and no other phosphorylation sites were detectably depleted, apart from PPP6R1 S531, in cells expressing PPP1R15B (Figure 2-S2A,B). Expression of the PP1-PNUTS fusion, which includes sequences that recruit WDR82 (Lee et al., 2010), led to specific depletion of phosphorylation sites from CXXC1/CFP1 and SET1B, which along with WDR82 are components of the COMPASS histone lysine *N*-methyl transferase complexes (Cenik and Shilatifard, 2021) (Figure 2-S2C). These proteins bear no obvious sequence similarity in the vicinity of the dephosphorylation site (Figure 2-S2D). These findings will be explored in future work.

New candidate substrates for Neurabin and Spinophilin

Having validated the PP1-PIP fusion approach, we focussed on Neurabin and Spinophilin, two PIPs implicated in neuronal plasticity (Sarrouilhe et al., 2006; Foley et al., 2021), which contain a PDZ domain implicated in recruitment of potential substrates (Burnett et al., 1998; Yan et al, 1999; Sarrouilhe et al., 2006; Kelker et al., 2007). The PDZ domain is separated from the RVxF-ΦΦ-R-W string by a 5-turn α-helix, which remodels the PP1 hydrophobic groove in a manner distinct from Phactr1 (Figure 1A, Figure 1-S2G)(Ragusa et al., 2010; Fedoryshchak et al., 2020).

Expression of the PP1-Neurabin or PP1-Spinophilin fusions led to specific depletion of closely related sets of phosphorylation sites (Figure 3A,3B). These included multiple sites from the translational inhibitor proteins 4E-BP1 and 4E-BP2. Levels of total 4E-BP1 and 4E-BP2 proteins were not affected (Figures 3-S1A). Phosphorylation sites from two other proteins, DTL and CAMSAP3, were also significantly depleted upon expression of both PP1-Spinophilin and PP1-Neurabin fusions, while a further 7 were specific to one fusion or the other (see Discussion). However, apart from a preference for proline at position +1, inspection these sequences did not reveal any obvious sequence similarities in the vicinity of the dephosphorylation site (Figure 3C). Substrates identified in the PP1-Phactr and PP1-PNUTS screens showed no detectable depletion, and *vice versa*, indicating that the substrates identified were specific for each fusion. Consistent with the phosphoproteomics data, immunoblotting analysis with phosphorylation-specific antibodies demonstrated that induction of PP1-Neurabin resulted in decreased phosphorylation of T70, S65/S101 and possibly T37/T46, while total 4E-BP1 resolved from a heterogeneous distribution to a largely monodisperse species (Figure 3D, Figure 3-S1B,C).

The 4E-BPs are critical components of the mTORC1 growth control pathway which couples translation to nutrient availability and extracellular signals (reviewed by Hoeffer and Klann, 2010; Liu and Sabatini, 2020) (see Discussion). Phosphorylation of 4E-BPs potentiates translation by inhibiting their ability to sequester EIF4E (reviewed by Martineau et al, 2013; Romagnoli et al, 2021). Accordingly, expression of PP1-Neurabin, but not PP1 alone, suppressed translation in 293 cells (Figure 3E). These data establish the Neurabin/PP1 and Spinophilin/PP1 holoenzymes as potential negative regulators of the mTORC1 pathway (Figure 3-S1D; see Discussion).

The PP1-Neurabin PDZ domain is required for 4E-BP1 dephosphorylation

To demonstrate a direct enzyme-substrate relationship between 4E-BP1 and PP1-Neurabin we expressed mCherry-tagged 4E-BP1 in 293 cells, recovered it on RFP-trap affinity beads, and incubated it with increasing amounts recombinant PP1-Neurabin. Analysis with the phospho-specific antibodies confirmed that pT37/46, pS65/101 and pT70 are all direct targets for dephosphorylation by PP1-Neurabin, with pT70 being somewhat preferred (Figure 4A, 4B). The 4E-BP C-terminal sequences are similar to those of p70 S6K, which was previously shown to interact with the Neurabin PDZ domain through a C-terminal PDZ binding motif (PBM) (Burnett et al., 1998) (Figure 4C). We therefore considered the possibility that 4E-BP1 dephosphorylation at multiple sites by PP1-Neurabin reflects its recruitment through PDZ interaction.

Simple deletion of the 4E-BP1 C-terminal residues substantially blocked phosphorylation of transfected mCherry-4E-BP1 (Figure 4-S1A), reflecting the loss of

the C-terminal TOR signalling (TOS) motif required for mTORC1 kinase recruitment and 4E-BP1 phosphorylation (Schalm and Blenis, 2002; Yang et al, 2017). Noting that the TOS motif does not include the C-terminal carboxylate, an essential part of the classical PBM (Harris and Lim, 2001; Tonikian et al, 2008; Subbaiah et al, 2011), we generated mCherry-4E-BP1(118+A): this contains an additional C-terminal alanine, which leaves the TOS motif intact but inactivates the PBM. Indeed, although mCherry-4E-BP1(118+A) was efficiently phosphorylated upon expression in 293 cells (Figure 4-S1A), its dephosphorylation *in vitro* required PP1-Neurabin concentrations some 20-50 times greater than the wildtype protein (Figure 4A, 4B). These results suggest that the 4E-BP1 C-terminal sequences constitute a PDZ binding motif (PBM), and point to a role for the Neurabin and Spinophilin PDZ domains in substrate recognition.

We next used a fluorescence polarization assay to compare the PDZ-binding affinity of the 4E-BP C-terminal sequences with those of p70 S6K, and other proteins reported to be Neurabin/Spinophilin PDZ ligands (Figure 4C)(Burnett et al., 1998; Penzes et al, 2001; Kelker et al., 2007; Ragusa et al., 2010). The 4E-BP1 PBM, which is identical amongst all three 4E-BP isoforms, bound the PDZ domains with comparable affinities in the micromolar range, and binding was abolished by substitution of the C-terminal hydrophobic residues (Figure 4C,4D; Figure 4-S1B). These binding affinities were 10-30-fold greater than those p70 S6K and the RhoGEF Kalirin-7, which were of order 100 μM, and >100-fold greater than various glutamate receptor C-terminal peptides (Figure 4C,4D; Figure 4-S1B). p70 S6K also functions in the mTORC1 pathway (for reviews see Liu and Sabatini, 2020; Artemenko et al, 2022). Although most of its phosphorylation sites were not detected by phosphoproteomics, immunoblotting experiments demonstrated that PP1-

Neurabin expression decreased levels of the activating T389 phosphorylation (Figure 4-S1C).

PDZ domain interaction determines PP1-Neurabin specificity

We next compared how interactions with the PP1-Neurabin PDZ and the remodelled PP1 hydrophobic groove contribute to substrate specificity. To do this we compared the ability of PP1-Neurabin and PP1-Phactr1 to dephosphorylate synthetic peptides derived from their substrates 4E-BP1 and IRSp53. In these peptides 14^{mer} sequences spanning 4E-BP1 and IRSp53 dephosphorylation sites are joined via a GSG linker to wildtype or mutant 4E-BP1 PBM sequences (Figure 5A). As a representative PP1-Neurabin substrate we used 4E-BP1 residues 64-78, including the phosphorylated T70 site, linked to intact or mutant 4E-BP1 PBM (substrates 4E-$BP1^{PBM}$ and 4E-$BP1^{MUT}$). For comparison, we used Phactr1 substrate peptides comprising IRSp53 residues 449-463, spanning the phosphorylated S455 site, also linked to the intact or mutant 4E-BP1 PBM (substrates $IRSp53^{PBM}$ and $IRSp53^{MUT}$; (Figure 5A, Figure 5-S1A). These substrates, or their mutated derivatives, were then dephosphorylated using PP1-Neurabin, PP1-Phactr1, or PP1 alone. Results are summarised in Figures 5 and 5S-1; the assay data and statistical analysis provided in Supplementary Table S3.

PP1-Neurabin dephosphorylated 4E-$BP1^{PBM}$ with a catalytic efficiency some 100-fold greater than PP1 alone, while peptide 4E-$BP1^{MUT}$, which cannot bind the Neurabin PDZ domain, was 30-fold less reactive (Figure 5B, Figure 5-S1A,B). In contrast, PP1-Phactr1 dephosphorylated 4E-$BP1^{PBM}$ and 4E-$BP1^{MUT}$ at rates similar to those achieved by PP1 alone (Figure 5B, Figure 5-S1A,B). The Neurabin

sequences, specifically the PDZ domain, thus play a critical role in specific 4E-BP1 pT70 substrate recognition. PP1-Neurabin also dephosphorylated IRSp53^{PBM}, which contains the 4E-BP1 PBM, with somewhat higher catalytic efficiency to that seen with 4E-BP1^{PBM} itself (Figure 5B, Figure 5-S1A,B). This was entirely dependent on PDZ domain interaction, IRSp53^{MUT} being ~100-fold less reactive (Figure 5B, Figure 5-S1A,B). In contrast, PP1-Phactr1 dephosphorylated both IRSp53^{PBM} and IRSp53^{MUT} peptides with a similar catalytic efficiency, some 100-fold greater than that seen with PP1 alone (Figure 5B, Figure 5-S1A,B). These results demonstrate the critical role played by the PDZ domain substrate specificity, and underscore the role played by PIPs in potentiating the catalytic efficiency of PIP/PP1 complexes.

Substrate interactions with the remodelled PP1 hydrophobic groove do not affect PP1-Neurabin specificity

We next assessed the potential role of the remodelled hydrophobic groove in substrate recognition. Positions +3 to +6 relative to the dephosphorylation site are critical for recognition of the remodelled hydrophobic groove by Phactr1/PP1 (Fedoryshchak et al., 2020), so we assessed the effect of mutations at these positions on catalytic activity. PP1-Neurabin dephosphorylated 4E-BP1^{PBM} containing alanine substitutions, or IRSp53 sequences, at positions +3/4 or +5/6 with slightly increased catalytic efficiency (Figure 5C, Figure 5-S1A,C). These mutations had strikingly different effects on 4E-BP1^{PBM} dephosphorylation by PP1-Phactr1, however. While the alanine substitutions at positions +3/4 or +5/6 had little effect, conversion of +4 to +6 to the IRSp53 sequence LLD increased catalytic efficiency some 20-fold (Figure 5C, Figure 5-S1A,C). Similar results were seen with the IRSp53 substrate peptides: alanine substitution in the groove-interacting region had

no effect on catalytic efficiency with PP1-Neurabin, but significantly impaired it with PP1-Phactr1 (Figure 5D, Figure 5-S1A,D). Strikingly, alanine substitutions at +1 and +2 in 4E-BP1^{PBM} significantly increased catalytic efficiency by both PP1-Neurabin and PP1-Phactr1, perhaps reflecting changes at the catalytic site itself (Figure 5E, Figure 5-S1A,E; see Discussion).

Taken together with the results in the preceding section, these data support a model in which PP1-Neurabin substrate specificity is driven predominantly by the ability of substrates to interact with the Neurabin PDZ domain rather than the remodelled PP1 hydrophobic groove (Figure 5-S2). In contrast the specificity of PP1-Phactr1, like that of the PP1/Phactr1 holoenzyme, is critically dependent on interaction with the remodelled PP1 hydrophobic groove (Fedoryshchak et al., 2020)(Figure 5-S2; see Discussion).

Structural analysis of PP1/Neurabin – 4E-BP1 interaction

We next sought to visualise PP1-Neurabin/4E-BP1 interactions directly at the structural level. To do this, we used the “c himera” strategy previously used to examine Phactr1/PP1/substrate interactions, in which Phactr1 substrate sequences were fused C-terminally to PP1(7-304), and co-crystallised with the Phactr1 PP1-interacting C-terminal domain. This revealed a putative enzyme-product complex, with substrate sequences binding in a remodelled PP1 hydrophobic groove and serine and a presumed phosphate docked at the active site (Fedoryshchak et al., 2020). Accordingly, we constructed an analogous PP1-4E-BP1 substrate fusion, comprising PP1(7-304) / $(SG)_5$ / 4E-BP1(65-83) / G / 4E-BP1(112-118) (Figure 6A), co-expressed it with Neurabin residues 423-593, and determined the crystal

structure of the purified complex at 2.36 Å resolution (Figure 6B, Figure 6-S1; Table 1) (Ragusa et al., 2010).

In the complex, the PP1 catalytic core and Neurabin PDZ sequences were well resolved, along with the 4E-BP1 PBM, which was docked with the Neurabin PDZ domain (Figure 6B). The individual domains were largely identical to those determined previously for unliganded Neurabin/PP1 (Ragusa et al., 2010) (PP1(1-304), RMSD 0.22 Å over 269 Cα, PDZ(501-592) RMSD 0.39 Å over 65 Cα). However, the PDZ domain in our Neurabin/PP1-4E-BP1 substrate complex structure is oriented at 22° to that in the unliganded Neurabin/PP1 complex, reflecting to a slight bend in the C-terminal section of the 5-turn α-helix that connects it to the RVxF-ΦΦ-R-W string (Figure 6C). The 4E-BP1 PBM, 113(QFEMDI)118, uses a beta-strand addition mechanism to make extensive contacts with the Neurabin PDZ domain, similar to those seen in other PDZ-ligand complexes, that widen the PBM-binding groove (Figure 6D, Figure 6-S1B): 4E-BP1 F114, M116 and I118 side chains make hydrophobic contacts, while their main chain carbonyl and amide groups, and the C-terminal carboxylate, form an extensive hydrogen bonding network with Neurabin main chain residues L514, G515, I516, I518, and G520 (Figure 6D).

Apart from the C-terminal PBM, the 4E-BP1 T70 substrate sequences were largely unresolved in the crystal structure. Unlike the Phactr1 substrate chimera, no interactions were seen with the remodelled PP1-Neurabin hydrophobic groove; and no virtual enzyme-product complex and solvent phosphate were detected at the active site, perhaps reflecting the absence of stabilising hydrophobic groove interactions (Figure 6B). To gain insight into potential interactions at the PP1 catalytic site, we therefore used AlphaFold3 to model the PP1-4E-BP1 substrate chimera in its phosphorylated and unphosphorylated states (Figure 6-S2A, 6-S2B).

While the 4E-BP1/ PDZ interaction was correctly predicted regardless of phosphorylation status (Figure 6E, Figure 6-S2E), only the phosphorylated substrate was predicted to interact directly with the PP1 active site. The 4E-BP1 substrate sequence ^{68}TK(pT70)PPR^{73}, predicted with high confidence, docks at the catalytic site, with K69 interacting with D220^{PP1}, pT70 interacting with the metal ions, H125^{PP1} and R221^{PP1}, and P71 interacting with Y134^{PP1}, but the remodelled PP1 hydrophobic groove remains unoccupied (Figure 6E, Figure 6-S2C). In contrast, AlphaFold3 gives only a low confidence prediction for the unphosphorylated substrate site D74 and L75 interacting with H125^{PP1}, and Y134^{PP1} (Figure 6-S2D).These results are consistent with the biochemical studies, and support the notion that interaction with the remodelled hydrophobic groove plays no part in recognition of 4E-BP1 by the Neurabin/PP1 holoenzyme.

Finally we used AlphaFold3 to predict interactions between Neurabin/PP1 and full-length 4E-BP1 phosphorylated on T37, T46, S65, T70, or S101 (Figure 6F, Figure 6-S2F). All the predictions placed the C-terminus of 4E-BP1 in the ligand-binding groove of the PDZ domain, docking the phosphorylated T70 site in the PP1 active site in a similar manner way to that seen in the substrate chimera predictions (Figure 6F; Figure 6-S2C). Taken together with the crystallography and biochemical data, our observations support the view that the primary determinant of substrate specificity for Neurabin/PP1 is interaction with the PDZ domain adjacent to the RVxF-ΦΦ-R-W string.

DISCUSSION

The PP1 catalytic subunit possesses little intrinsic sequence specificity. Instead it recognises specific substrates by forming holoenzymes in which it partners with a variety of PP1 interacting proteins (PIPs) to direct dephosphorylation to specific substrates. We previously showed that interaction of the Phactr1 PIP with PP1 remodels the PP1 hydrophobic substrate groove in such a way as to allowing specific recognition of substrate sequences C-terminal to the dephosphorylation site (Fedoryshchak et al., 2020). Phactr1 belongs to a group of PIPs that recognise PP1 using a common RVxF-ΦΦ-R-W string, all of which potentially remodel the hydrophobic groove; indeed, structural studies confirm that Neurabin and Spinophilin (PPP1R9A, PPP1R9B) do this differently from the Phactrs (Ragusa et al., 2010; Fedoryshchak et al., 2020). We identified potential substrates for the other RVxF-ΦΦ-R-W PIPs, and elucidate mechanisms of substrate recognition, focussing on the Neurabin and Spinophilin PIPs.

Our previous study showed that a fusion protein comprising PP1 joined to Phactr1 sequences C-terminal to the RVxF motif maintains both the structure and the sequence-specificity of the intact Phactr1/PP1 holoenzyme (Fedoryshchak et al., 2020). We used this fusion approach, in conjunction with MS phosphoproteomics in 293 cells, to compare the specificities of the different Phactr family members, and to identify potential substrates for other RVxF-ΦΦ-R-W PIPs. All four PP1-Phactr fusions exhibited virtually identical substrate specificities, which were substantially similar to that of the authentic Phactr1/PP1 holoenzyme, giving confidence that findings made with the fusions are also applicable to other RVxF-ΦΦ-R-W PIP/PP1 holoenzymes. It is likely that differential intracellular targeting and/or tissue-specific

expression of the four different Phactr/PP1 holoenzymes allows further refinement of substrate specificity.

Expression of the other PP1-(RVxF-ΦΦ-R-W PIP) fusions revealed potential substrates for PNUTS and PP1-Neurabin/-Spinophilin. Unlike the PP1-Phactr substrates, however, these exhibited no obvious sequence similarities in the substrate sequences adjacent to the targeted dephosphorylation remodelled hydrophobic groove. For PNUTS, we identified only the SET1A/B-COMPASS complex components CXXC1/CFP1 and SETD1B (Cenik and Shilatifard, 2021). These may be recruited to PNUTS by interaction with its binding partner WDR82, which is also present in SET1A/B-COMPASS complexes (Cenik and Shilatifard, 2021), but further work will be necessary to confirm this. We did not recover potential substrates for PP1-PPP1R15A/B. It is possible that the use of the PP1 fusion approach for these PIPs is confounded by interaction of these PIPs with G-actin (Chen et al., 2015; Yan et al., 2021).

Expression of the PP1-Neurabin and PP1-Spinophilin fusions identified nine potential substrates with eighteen candidate dephosphorylation sites, of which eight represented conserved mTORC1 dependent phosphorylations of the translational regulators 4E-BP1 and 4E-BP2. Using immunoblotting we found that the p70 S6K activating phosphorylation at T389 also appears to be a substrate for PP1-Neurabin. The 4E-BPs and p70 S6K are critical targets of the mTORC1 pathway, which links translational control to cell nutrient status and extracellular signals in multiple settings (Hoeffer and Klann, 2010; Liu and Sabatini, 2020). Consistent with this, we found that overexpression of PP1-Neurabin can suppress translation when expressed in 293 cells. It therefore is likely that Neurabin and Spinophilin can

negatively regulate both arms of the mTORC1 protein synthesis pathway (Figure 3-S1C).

The presence of multiple dephosphorylation sites on the 4E-BPs with no obvious primary sequence homology raised the question of how these targets are recognised. We found that dephosphorylation of 4E-BP1 by PP1-Neurabin requires its C-terminal sequences, which constitute a classical PDZ-binding motif (PBM) (Harris and Lim, 2001; Tonikian et al., 2008; Subbaiah et al., 2011). The micromolar affinity of this interaction, which is stronger than that previously reported for p70 S6K (Burnett et al., 1998), may reflect the necessity for effective competition with the mTORC1 kinase complex, which binds the 4E-BPs using a C-terminal TOS motif that overlaps the PBM (Schalm and Blenis, 2002; Yang et al., 2017). Although we recovered a number of other potential Neurabin and Spinophilin substrates in the proteomics screen, none contains an obvious potential C-terminal PBM; further work will be necessary to establish whether they are *bona fide* substrates. We found that other reported ligands, such as the glutamatergic and dopaminergic receptors (Kelker et al., 2007) bind the Neurabin/Spinophilin PDZ domains with much lower affinity than 4E-BP1 or even p70 S6K. In neurons, association of these receptors with Neurabin and PP1 correlates with channel activity and dephosphorylation (Wu et al, 2008; Yan, 1999 #29, reviewed by Foley et al., 2021). It may be that Neurabin/Spinophilin oligomerisation and/or F-actin binding, and membrane localisation, effectively increases the avidity of such weak PBM-PDZ interactions, but more work is required to establish whether these channels are direct Neurabin/PP1 substrates.

We used synthetic peptide substrates derived from 4E-BP1, or the Phactr1/PP1 substrate IRSp53, to investigate how the substrate recognition

mechanisms differ between the PP1-Neurabin and PP1-Phactr fusions. In the context of the PP1-PIP fusions, and by extension in that of the PIP/PP1 holoenzyme, the PIP sequences play a critical role in directing substrate specificity and potentiating catalytic efficiency. In the PP1-Neurabin fusion, interaction with the PDZ domain is the critical determinant of both catalytic efficiency and specificity (Figure 5-S2). It increases catalytic efficiency 100-fold above that seen with PP1 alone, or the PP1-Phactr1 fusion. Moreover, the PP1-Neurabin fusion was inactive with the Phactr1/PP1 substrate IRSp53 unless the latter was made competent to bind the Neurabin PDZ domain. Our observations suggest a model in which 4E-BPs are recruited to Neurabin/PP1 via high affinity PBM-PDZ interaction, with the relatively low affinity of active-site interaction allowing dephosphorylation of the multiple sites during one round of PDZ binding (Figure 5-S2). In contrast, dephosphorylation of the Phactr1/PP1 target IRSp53 pS455 by the PP1-Phactr1 fusion protein was critically dependent on interaction with the remodelled hydrophobic groove, consistent with our previous data (Figure 5-S2)(Fedoryshchak et al., 2020).

Several lines of evidence support the view that interaction with the remodelled PP1 hydrophobic groove plays no role in PP1-Neurabin substrate recognition. First, the PP1-Neurabin substrates we identified have no obvious sequence similarity at positions +3 to +6, the sequences that potentially interact with the remodelled hydrophobic groove, and alanine substitutions at these positions do not influence PP1-Neurabin catalytic activity. Structural analysis of a PP1-4E-BP1 substrate fusion complexed with Neurabin, also revealed no substrate contacts with PP1, although the PDZ-4E-BP1 interaction was well-resolved. Finally AlphaFold modelling of complexes formed between 4E-BP1 substrates and the Spinophilin/PP1 holoenzyme predicted phosphorylation-specific interactions with the PP1 catalytic site, but no

interactions with the remodelled hydrophobic groove. We were intrigued to note, however, that alanine substitutions at +1 and +2 in relative to 4E-BP1 pT70 increased reactivity with both PP1-Neurabin and PP1-Phactr1. We speculate that this “suboptimal” reactivity may reflect a requirement to balance dephosphorylation rates between the multiple 4E-BP1 phosphorylation sites, especially if multiple rounds of dephosphorylation occur for each PBM-PDZ interaction.

Although the remodelled hydrophobic groove does not play a role in 4E-BP recognition by Neurabin/PP1, this does not necessarily mean that sequence-specific dephosphorylation by other PIP/PP1 complexes and substrate recruitment by protein interactions are inherently mutually exclusive: in principle a PIP could recruit substrates through protein interactions, and remodel the PP1 substrate binding grooves to allow discrimination between different phosphorylated sites on the target protein. That said, we think it likely that the other RVxF-ΦΦ-R-W PIPs will also recruit substrates by interaction with other PIP domains, or proteins bound to them. Such interactions might involve WDR82 for PNUTS, and G-actin for PPP1R15A/B (Yan et al., 2021; Erickson et al, 2024).

Our findings establish Neurabin/PP1 and Spinophilin/PP1 holoenzymes as new candidate regulators of the mTORC1 pathway. Many studies have focussed on mTORC1 regulation of translation on the control of cell growth, particularly in cancer settings (Liu and Sabatini, 2020), and previous work has shown that endogenous PP2Cγ/ PPM1G contributes to 4E-BP1 dephosphorylation in 293 and HCT116 cells (Liu et al, 2013). Localised translational regulation is also important in other settings, however, including neuronal development and function (Holt et al, 2019). Here, mTORC1 signalling plays an important role in neuronal plasticity (Hoeffer and Klann, 2010), as do both Neurabin and Spinophilin, which are largely neuron specific and

enriched in dendritic spines (Wu, 2008 #75, reviewed by Foley et al., 2021), and the 4E-BPs, particularly 4E-BP2 (for references see Aguilar-Valles et al, 2015). Our finding that 4E-BPs are Neurabin/PP1 substrates potentially establishes a direct link between Neurabin and neuronal mTORC1 signalling (Figure 3-S1C), which will be an interesting topic for future investigation.

METHODS

Plasmids

NEBuilder HiFi DNA Assembly Cloning Kit and NEB Q5® Site-Directed Mutagenesis Kit were used according to manufacturer's protocols for plasmid assembly and mutagenesis. All primers are listed in Supplementary Table S1.

PIP sequences were amplified from 293 cells cDNA, except for the Neurabin sequence which was commercially synthesized. pET28-PP1(7-300) and pET28-PP1(7-304)-SGSGS-Phactr1(526-580) Phactr1 plasmids were as described (Fedoryshchak et al., 2020). Other fusion proteins were expressed pET28-based expression plasmids were used to express other PP1-PIP fusions as follows: PP1(7-304)-SGSGS-Phactr2(580-634); PP1(7-304)-SGSGS-Phactr3(505-559); PP1(7-304)-SGSGS-Phactr4(648-702); PP1(7-304)-SGSGS-Neurabin(464-610); PP1(7-304)-SGSGS-Spinophilin(456-602); PP1(7-304)-SGSGS-R15A(562-674); PP1(7-304)-SGSGS-R15B(647-713); PP1(7-304)-SGSGS-PNUTS(408-619).

For T-Rex cell lines, pOG44 (Thermo) and pcDNA5/FRT/TO plasmids (Thermo) were used in conjunction with N-terminally Flag-tagged PP1-PIP fusions were inserted into pcDNA5/FRT/TO.

pcDNA3.1 IRSp53 and pcDNA3.1 IRSp53 L460A were as described (Fedoryshchak et al., 2020). To obtain pEF mCherry-4E-BP1, the 4E-BP1 sequences were amplified from 293 cells and inserted into pEF-mCherry plasmid. Site-directed mutagenesis was used to derive mutants ΔPDZ, 118+A, S65A, S101A, S65A/S101A. pGEX-Neurabin(PDZ) and pGEX-Spinophilin(PDZ) plasmids were obtained by cloning Neurabin and Spinophilin PDZ domains into the pGEX 6P2

vector (GE Healthcare). The PP1-4E-BP1 chimera was generated by insertion of 4E-BP1 sequences into pET28-PP1.

Cell lines and transfections

Commercially available 293 Flp-In T-REx cells and pOG44 + pcDNA5/FRT/TO stably transfected derivatives were used throughout. Cells were maintained in a humidified incubator at 37°C and 5% CO_2 and cultured in DMEM (Gibco) supplemented with 10% FCS (Gibco) and penicillin-streptomycin (Sigma). Prior to stable transfection, 293 Flp-In T-REx cells were maintained with 100 mg/mL Zeocin (Invivogen). Stably transfected 293 Flp-In T-REx derivative cell lines were cultured in a medium supplemented with 5 mg/mL Blasticidin (Invivogen) and 100 mg/mL Hygromycin B (Invivogen).

For stable transfection of a PP1-fusion protein, pOG44 and pcDNA5/FRT/TO-PP1-fusion plasmids were mixed at a ratio of 9:1. Lipofectamine™ 2000 (Invitrogen) in Opti-MEM® (Gibco) was added and transfection was done following the manufacturer's protocol. 100 µg/mL Hygromycin B (Invitrogen) was added to start the selection of stable cell line 2 days after transfection. Selection was complete and cell line stocks were frozen after 14 days.

pEF IRSp53 and pEF-mCherry-4E-BP1 plasmids were transfected with Lipofectamine™ 2000 (Invitrogen) in Opti-MEM® (Gibco) following the manufacturer's protocol. Cells were lysed 1 day after transfection in a buffer containing 20 mM Tris pH 7.4, 150 mM NaCl, 1 mM EDTA, 1 mM EGTA, 1% Triton X-100, 10% glycerol, 0.2% SDS. Lysates were cleared by centrifugation. 4x LDS sample buffer supplemented with DTT was added before running Immunoblots.

Unless otherwise indicated, 1000 nM of tetracycline was used to express the PP1 fusion proteins in stably transfected 293 Flp-In T-REx cells, and the experiments were performed 16 h post-induction.

Immunoblotting

SDS-PAGE analysis of cell lysates and immunoblotting was performed using standard techniques; the signal was visualised and quantified using Odyssey CLx instrument (LI-COR) and the Image Studio (LI-COR) Odyssey Analysis Software. Primary antibodies used were Flag (1:2000, clone M2, Sigma F7425, mouse), IRSp53 (1:1000, Abcam ab15697), IRSp53 pS455 (1:500, previously described in Fedoryshchak 2020), Afadin (1:200, Santa Cruz sc-74433), Afadin pS1275 (1:500, previously described in Fedoryshchak 2020), Gapdh (1:2000, clone 0411, Santa Cruz sc-47724), 4E-BP1 (1:1000, Cell Signalling 9452), 4E-BP1 pT37/46 (1:1000, Cell Signalling 9459), 4E-BP1 pS65 (1:1000, Cell Signalling 9451), 4E-BP1 pT70 (1:1000, Cell Signalling 9455), mCherry (1:1000, clone 16D7, Thermo M11240, rat), S6K (1:1000, Cell Signalling 9202), S6K pS371 (1:1000, Cell Signalling 9208), S6K pT389 (1:1000, Cell Signalling 9205), S6K pT421/pS424 (1:1000, Cell Signalling 9204). Secondary antibodies labelled with IRDye 800CW and IRDye 680LT were from LI-COR.

Proteomics

Total and phospho-proteomics experiment was performed according to a detailed protocol previously published (Jones et al, 2020). Cells expressing PP1-PIP fusion proteins, PP1 only, or vector alone were induced with tetracycline for

16h.Cells were lysed in buffer containing 8 M Urea, 50 mM HEPES pH 8.5, 10 mM Glycerol 2-phosphate, 50 mM NaF, 5 mM Sodium pyrophosphate, 1 mM EDTA, 1 mM Sodium vanadate, 1 mM dithiothreitol, 1:50 protease inhibitor cocktail (Roche), 1:100 Phosphatase inhibitor cocktail, 400 nM Okadaic acid. Cysteines were reduced and alkylated by iodoacetamide followed by trypsin/rLysC protease digestion. Peptide samples were labelled with 10-plex (UK288606) and additionally 131C (VC294053) TMT reagents from Thermo and pooled. Part of the sample was injected saved for the total proteome analysis. The rest of the sample was used for 2-step phosphopeptide enrichment on TiO_2 beads (Thermo) and FeNTA beads (Thermo). Phosphopeptides were fractionated. Total proteome and enriched phosphopeptide fractions were separated on a 50 cm, 75 µm I.D. Pepmap column over a 2 h gradient and eluted directly into the Orbitrap Fusion Lumos, operated with Xcalibur software, with measurement in MS2 and MS3 modes. The instrument was set up in data-dependent acquisition mode, with top 10 most abundant peptides selected for MS/MS by HCD fragmentation.

Raw mass spectrometric data were processed in MaxQuant (version 1.6.12.0); database search against the *Homo sapiens* canonical sequences from UniProtKB was performed using the Andromeda search engine. Fixed modifications were set as Carbamidomethyl (C) and variable modifications set as Oxidation (M), Acetyl (Protein N-term) and Phospho (STY). The estimated false discovery rate was set to 1% at the peptide, protein, and site levels, with a maximum of two missed cleavages allowed. Reporter ion MS2 or Reporter ion MS3 was appropriately selected for each raw file.

Phosphorylation site tables were imported into Perseus (v1.6.14.0) for analysis. Contaminants and reverse peptides were cleaned up from the

Phosphosites (STY) and the values normalised and averaged between MS2 and MS3 datasets using Z-score function across columns. All samples were analysed as triplicates, except PP1-Spinophilin and PP1-PNUTS, for which duplicates were used due to the presence of an outlier dataset as determined by principal component analysis. Phosphorylation site enrichments were compared using multiple t-test with permutation based false-discovery cutoff at 5% unless indicated otherwise. Enrichment data are summarised in Supplementary Table S2.

Mass spectrometry proteomics data have been deposited to the ProteomeXchange Consortium via the PRIDE partner repository with the dataset identifier PXD055166.

Peptides

Peptides were synthesized by the Francis Crick Institute Chemical Biology Science Technology Platform using standard Fmoc-SPPS techniques.

Name	**Sequence** (FAM, 6-Carboxyfluorescein; eahx, aminohexanoic acid linker; OH, carboxyl at C-terminus
4EBP	FAM-eahx-QFEMDI-OH
4EBP-mut	FAM-eahx-QFESGS-OH
S6K	FAM-eahx-EHLRMNL-OH
Kalirin-7	FAM-eahx-DPFSTYV-OH
GluR1	FAM-eahx-LGATGL-OH
GluR2	FAM-eahx-IESVKI-OH
GluN1-1	FAM-eahx-SVSTVV-OH
GluN2A	FAM-eahx-SIESDV-OH
4E-BP1^{PBM}	Ac-NSPVTK(**pT**)PPRDLPTIGSGSQFESGS**-OH**
4E-BP1$^{LLD-PBM}$	Ac-NSPVTK(**pT**)PPR**L**L**D**TIGSGSQFEMDI**-OH**
IRSp53^{PBM}	Ac-QQGKSS(**pS**)TGNLLDKDGSGSQFEMDI**-OH**
IRSp53^{MUT}	Ac-QQGKSS(**pS**)TGNLLDKDGSGSQFESGS**-OH**
IRSp53^{5A-PBM}	Ac-QQGKSS(**pS**)TGNL**A**DKDGSGSQFEMDI**-OH**
IRSp53^{5A-MUT}	Ac-QQGKSS(**pS**)TGNL**A**DKDGSGSQFESGS**-OH**
4E-BP1$^{12A-PBM}$	Ac-NSPVTK(**pT**)**AA**RDLPTIGSGSQFEMDI**-OH**

4E-BP1$^{34A\text{-}PBM}$	Ac-NSPVTK(**pT**)PP**AA**LPTIGSGSQFEMDI**-OH**
4E-BP1$^{56A\text{-}PBM}$	Ac-NSPVTK(**pT**)PPRD**AA**TIGSGSQFEMDI**-OH**
4E-BP1$^{1A\text{-}PBM}$	Ac-NSPVTK(**pT**)**A**PRDLPTIGSGSQFEMDI**-OH**
4E-BP1$^{2A\text{-}PBM}$	Ac-NSPVTK(**pT**)P**A**RDLPTIGSGSQFEMDI**-OH**

Protein expression and purification

PP1-fusion proteins were produced as 6xHis-tagged fusion proteins in (DE3) *E. coli* cells (Invitrogen) with pGRO7 co-expression as described (Choy et al., 2014). Overnight pre-cultures (400ml) were grown in LB medium supplemented 1 mM $MnCl_2$ and used to inoculate a 100L fermenter. After growth to OD_{600} of ~0.5, 2 g/L of arabinose was added to induce GroEL/GroES expression. At OD_{600} ~1, the temperature was lowered to 17°C and protein expression induced with 0.1 mM IPTG for ~18 hours. Cells were harvested, re-suspended in fresh LB medium/1mM $MnCl_2$/200 µg/ml chloramphenicol and agitated for 2h at 17°C. Harvested cells were resuspended in lysis buffer (50 mM Tris-HCl, pH 8.5, 5 mM imidazole, 700 mM NaCl, 1mM $MnCl_2$, 0.1% v/v TX-100, 0.5 mM TCEP, 0.5 mM AEBSF, 15 µg/ml benzamidine and complete EDTA-free protease inhibitor tablets), lysed by French press, clarified, and stored at -80°C.

Clarified lysates were loaded onto a 5ml HisTrap crude column on an AktaPure HPLC, washed with 20CV of buffer A (25 mM Tris-HCl pH 8.5, 250 mM NaCl, 10mM imidazole pH 8, 1mM $MnCl_2$), His-tagged fusion proteins were eluted in buffer B (Buffer A + 240mM Imidazole) and purified using size exclusion chromatography on a Superdex 200 26/60 column in SEC buffer1 (25 mM Tris-HCl pH 8.5, 200 mM NaCl, 0.5mM TCEP, 10 mM imidazole). The His tag was then cleaved off by incubating overnight with His-Tev protease at 4°Cm and the cleaved product recovered by passage of the sample over a 5ml HisTrap crude column. Protein was then concentrated and further purified on a Superdex 75 equilibrated in SEC buffer2 (25

mM Tris-HCl pH 8.5, 200 mM NaCl, 0.5mM TCEP). The PP1-Fusion proteins were concentrated to 10 mg/ml and stored at -80ºC.

His-tagged Neurabin and Spinophilin PDZ domains were produced in BL21 (DE3) *E. coli* cells (Invitrogen). Overnight pre-cultures were grown in LB medium, 15 ml was used to inoculate 1L of TB media in a 2L baffled flasks. When OD_{600} =1, the temperature was lowered to 20°C and protein expression induced by addition of 0.1 mM IPTG for ~18 hours. Harvested cells were resuspended in lysis buffer (50 mM Tris-HCl, pH 8.5, 5 mM imidazole, 700 mM NaCl, 0.1% v/v TX-100, 0.5 mM TCEP, 0.5 mM AEBSF, 15 µg/ml benzamidine and complete EDTA-free protease inhibitor tablets), lysed by French press, clarified, and stored at -80°C. PDZ domains were purified using the same protocol as PP1-fusion proteins without addition of 1mM MnCl2 in the buffers.

Crystallisation and structure determination

PP1-4E-BP1/Neurabin was concentrated to 10 mg/ml and crystallised at 20°C using sitting-drop vapour diffusion. Sitting drops of 1 µl consisted of a 1:1 (vol:vol) mixture of protein and well solution (20% PEG 6000, 0.2M $MgCl_2$, 0.1 M MES pH 6.0). Crystals appeared within 5 days and reached maximum size after 7 days. Crystals were cryoprotected in well solution supplemented with 15% Glycerol + 15% ethylene glycol and flash-frozen in liquid nitrogen. 100 K at beamlines I04 (mx25587-44) of the Diamond Light Source Synchrotron (Oxford, UK). Data collection and refinement statistics are summarized in Table 1. Data sets were indexed, scaled and merged with xia2 (Winter et al, 2013). Molecular replacement used the atomic coordinates of human PP1 from PDB 4M0V (Choy et al., 2014) in PHASER (McCoy et al, 2007).

Refinement used Phenix (Adams et al, 2010). Model building used COOT (Emsley et al, 2010) with validation by PROCHECK (Vaguine et al, 1999). Two copies of the complex were modelled in the asymmetric unit, but the entire PDZ domain of one copy was poorly defined in the density and therefore not modelled. The same issue was previously observed for the unliganded Spinophilin/PP1 structure (Ragusa et al., 2010). For structure analysis we used the second copy of the complex showing well-resolved density for PP1-4E-BP1 chimera and Neurabin. AlphaFold3 predictions (Abramson et al, 2024) were performed using the AlphaFold3 server. Output structure prediction and parameter files are presented in Supplementary Data File 1.

Fluorescence polarisation assay

FAM-labelled peptides were dissolve in a buffer 25 mM Tris-HCl pH 8, 250 mM NaCl, 0.5 mM TCEP. Peptide concentration was measured using Thermo Scientific NanoDrop One by FAM fluorescence at 495 nm. FP assays (10 µl final volume) were performed in 384-well plates. 2 µl of 500 nM peptide solutions were added to each well (100 nM final concentration). 8 µl of Neurabin PDZ or Spinophilin PDZ was added as a serial dilution, starting at 1000 µM (800 µM final concentration). Anisotropies were read out on BMG Labtech CLARIOstar Plus microplate reader. Binding constants were estimated in GraphPad Prism 8 by fitting readouts with the following equation:

$$A = A_f + (A_b - A_f) * (K_d + L + C - \frac{(K_d + L + C)^{0.5}}{2 * L})$$

(A, anisotropy measured; A_f, anisotropy of free peptide; A_b, anisotropy of bound peptide; L, labelled peptide concentration; C, Protein concentration (X axis); K_d, binding constant).

Phosphatase activity assays

Phosphopeptides were dissolved in 25 mM Tris-HCl pH 8, 250 mM NaCl buffer. Peptide concentration was measured using DeNovix DS-11 based on absorbance values at 215 nm. Assays (10 µl final volume) were performed in 384-well plates. The activity of the PP1 fusion preparation was established on the day of each experiment, using 50 µM pIRSp53^{PBM} peptide as standard, with PP1-Phactr1 and PP1-Neurabin at various dilutions.

Peptides (4 µl) were serially diluted 2-fold from 1mM in complex buffer (1 mM $MnCl_2$, 25 mM Tris-HCl pH 8, 250 mM NaCl, 0.5 mM TCEP). 2 µl of 5x Phosphate sensor (Thermo) was added to the wells. 2 µl of PP1-fusion protein was added to the wells and fluorescence measurements were started immediately and taken every 3 min or 5 min using BMG Labtech CLARIOstar Plus microplate reader. Data was collected for 15 min at room temperature. Phosphate standards were measured to convert fluorescence readouts into phosphate concentration using a standard curve. Difference in fluorescence between the last and first data point was used as a readout.

A concentration of PP1-Phactr1 and PP1-Neurabin was chosen such that readouts were in the linear range of the Phosphate sensor detection. To measure K_M and catalytic efficiency (CE), an assay with varying dilutions of phosphopeptides was set up. 4 µl of a corresponding peptide dilution was added to wells, followed by 2 µl of 5x Phosphate sensor. 2 µl of PP1-fusion protein was added to the wells and fluorescence measurements were started immediately and taken every 3 min (alternatively, every 5 min). Data was collected for 15 min at room temperature.

Phosphate standards were measured to convert fluorescence readouts into phosphate concentration using a standard curve. Difference in fluorescence between the last and first data point was used as a readout. Rate constants were estimated in GraphPad Prizm 8 by fitting readouts to the rearranged Michaelis-Menten equation:

$$\frac{P}{t * E} = [\frac{k_{cat}}{K_M}] * \frac{C}{(\frac{C}{K_M} + 1)}$$

(P, phosphate released per time t; E, PP1-fusion concentration; [k_{cat}/K_M], catalytic efficiency; C, initial phosphopeptide concentration; K_M, Michaelis constant). Significance comparisons between activities with different peptides, or between different enzymes for the same substrate peptide were calculated using two-tailed two-sample equal variance Student's t-test. The assay data are presented in Supplementary Table S3.

4E-BP1 dephosphorylation immunoblot assay

293 Flp-In T-REx cells were transfected with mCherry-4E-BP1 (WT or 118+A mutant). Cells were lysed on the following day in the Tris-Triton buffer (see above). mCherry tagged constructs were enriched from the lysates using RFP-trap magnetic agarose beads (ChromoTek, rtma-20) using manufacturer's protocol. Enriched fractions were eluted from the beads with 500 µl 200 mM glycine pH 2.5, resulting in pure phosphorylated solution of mCherry-4E-BP1 (WT or 118+A mutant). Serial dilutions of PP1-Neurabin (0-1000 nM final concentration) were added to 40 µl aliquots of mCherry-4E-BP1 (WT or 118+A mutant) 8 µl and incubated for 15 min at room temperature before addition of 18 µl 4x LDS sample buffer with DTT. The samples were warmed to 70°C for 10min before analysis by immunoblotting.

Protein synthesis assay

293 Flp-In T-Rex cells were culture in a 6-well plate. PP1, PP1-Neurabin or vector construct expression were induced 16 h before the experiment with 1 μM tetracycline. Rapamycin was used at 50 nM for 16 h. *O*-propargyl puromycin (OPP; 5 μM) was added to the culture for 30 min. Then cells were washed once with PBS and resuspended using trypsin. Cells were collected by centrifugation at 300g for 5 min, then washed once with PBS and 4% PFA was added for 15 min. Cells were collected and resuspended in 0.5% Triton-X100 in PBS for 15 min. Cells were collected and resuspend in 2% BSA in PBS twice. Click-reaction mixture was prepared as follows: 1540 μL of water, 200 μL of 10x PBS, 40 μL CuSO4 (20mM) and BTTAA (100mM) mixture, 20 μL of 5 mM AlexaFluor-488 azide, 200 μL 100 mM sodium ascorbate.

200 μL of click-reaction mixture was added to each sample and incubated for 30 min in the dark. Cells were collected and resuspended in 10 mM EDTA. Then cells were incubated for 30 min in H33342 1:10000 in PBS. Cells were washed with PBS and analysed on BD LSRFortessa Cell Analyzer. FlowJo software was used to analyse flow cytometry data. Single cells readouts were isolated using forward and side scatter parameters. Mean fluorescent intensity in AlexaFluor-488 channel was used as assay readout.

ACKNOWLEDGEMENTS

We thank Sila Ultanir for helpful discussions, insights into neuronal plasticity, and support for pilot experiments in neurons, and lab members, Neil McDonald, and Sila Ultanir for helpful discussions and comments on the manuscript. We thank Helen Flynn from Crick Proteomics STP for assistance with phosphoproteomics experiments, Jo Redmond from Chemical Biology STP for help discussions about substrate specificity assistance with peptide synthesis, and Simone Kunzelman from the Structural Biology STP for assistance with FP assay. This work was supported by the Francis Crick Institute which receives its core funding from Cancer Research UK (CC2102), the UK Medical Research Council (CC2102), and the Wellcome Trust (CC2102). This research was funded in whole, or in part, by the Wellcome Trust CC2102. For the purpose of Open Access, the author has applied a CC BY public copyright licence to any Author Accepted Manuscript version arising from this submission. The authors have no conflicts of interest.

AUTHOR CONTRIBUTIONS

ROF designed the fusion proteins, constructed the fusion protein cell lines, and designed and conducted the proteomics and biochemical analysis. SM supervised the structural studies, designed the PP1-substrate fusions, and conducted crystallography and AlphaFold3 modelling experiments. KE-B performed protein expression and crystallography. DJ designed and synthesised peptides. ROF and RT conceived the project, designed and interpreted experiments, and wrote the paper, with input from other authors.

FIGURE LEGENDS

Figure 1. PP1-PIP fusion proteins.

A. Structures of fusion proteins. N-terminally Flag-tagged PP1α(7-304) is linked to sequences from each of the four families of RVxF-ΦΦ-R-W PIPs, shown as an open box. Each fusion contains sequences immediately C-terminal to the PP1 interaction motif (coloured lines) including known protein interaction domains previously implicated in potential substrate interactions (coloured blocks). For PIP sequences in each fusion see Figure 1-S1A and Methods.

Middle, sequences of the RVxF-ΦΦ-R-W string in each PIP, with motifs coloured. Each fusion contains the sequences C-terminal to the dashed line, represents the position of PP1-SGSGS linker insertion.

Bottom, structures of PP1/PIP complexes. Crystal structures of different PIP/PP1 complexes superimposed, aligned on PP1. Grey: PP1 (PDB: 4MOV), with PIP sequences as follows: green, Phactr1 (PDB: 6ZEE); magenta, Neurabin (PDB: 3HVQ); orange, R15A (PDB: 7NZM); blue, PNUTS (PDB: 4MOY). Dashed line, GSGSG linker.

B. Activity of PP1-Phactr1 expressed in Flp-In T-Rex 293 cells. PP1-Phactr1 expression was induced by tetracycline as indicated. Phosphorylation of Phactr1/PP1 substrates IRSp53 S455 and Afadin S1275 is shown below.

C. Analysis of Phactr1/PP1 substrate Afadin pS1275 phosphorylation in Flp-In TRex 293 cells expressing PP1 and PP1-fusion proteins.

Figure 1-S1.

A. PIP sequences in each fusion. Sequences of the PP1-binding and C-terminal sequences in each RVxF-ΦΦ-R-W PIP fusion are shown. Blue line indicates fusion point. Known interaction domains are overlined.

B. IRSp53 WT or L460A mutant were transfected into 293 Flp-In T-Rex cells expressing the different fusion proteins, and fusion expression induced by tetracycline. Immunoblotting for total and S455-phosphorylated IRSp53 is shown. Flag tag indicates expression of the fusion phosphatases. For each of the four PP1-Phactr fusions, the IRSp53 L460A peptide is significantly less reactive than the IRSp53WT peptide ($p<0.05$ for each fusion). Since the specificity of the four PP1-Phactr fusions is the same, combination of data for all four fusions is shown at the right. Bars are plotted as averages of 3 or 4 replicates. Statistical significance by Student's *t*-test: *, $p < 0.05$; ***; $p < 0.001$ - ****; $p < 0.0001$.

Figure 1-S2

A. Crystal structure of the PP1/Phactr1 complex (PDB 6ZEE). PP1 in white surface representation, with the hydrophobic substrate groove residues C127, A128, S129, I130, I133, Y134, V195, L205, W206, V223 coloured in grey, and PP1 active site presumptive Mn^{2+} ions in purple spheres. Phactr1 is in green surface representation.

B. Crystal structure of the PP1/Spinophilin complex (PDB 3EGG). A, and Spinophilin shown in light pink surface representation.

C. Crystal structure of the PP1/Neurabin complex (PDB 3HVQ). PP1 is shown as in A, and Neurabin shown in red surface representation.

D. Crystal structure of the PP1/PNUTS complex (PDB 4MOY). PP1 is shown as in A, and PNUTS shown in blue surface representation.

E. Crystal structure of the PP1/R15A/Actin/DNAse1 complex (PDB 7NZM). PP1 is shown as in A, and R15A shown in wheat surface representation, and actin as yellow ribbons.

F. Crystal structure of the PP1/R15B complex (PDB 4V0X). PP1 is shown as in A, and R15B shown in orange surface representation.

G. Superposition of all the PIP/PP1 complex structures shown in A-F. A close-up for the PP1 hydrophobic groove is shown, with PP1 as in A and each PIP shown as ribbon representation, coloured as in panels A-F, with the W motif residues shown in sticks.

H. Same as **F** in a different orientation to highlight the alterative orientations of the W PP1/R15A/Actin/DNAse1 and PP1/R15B complexes.

Figure 2. **PP1-PIP fusion phosphoproteomics.**

A. TMT phosphoproteomics workflow.

B. Average sample-to-sample correlations between triplicates from cells expressing the different fusion proteins, PP1α(7-304)-SGSGS alone, or empty vector. For the same fusion-expressing cell lines, the average of Pearson coefficients of correlation within a triplicate are shown.

C. Specific phosphosite depletion in cells expressing PP1-Phactr1 as opposed to PP1 alone. Abundances of specific phosphosites in PP1 and PP1-Phactr1 samples were determined, log-transformed, and expressed as Z-scores. For each phosphosite, depletion in cells expressing PP1-Phactr1 as opposed to PP1 alone

was quantified as the difference between the PP1 and PP1-Phactr1 Z-scores, and plotted versus -$\log_{10}$P. Dashed line, 5% false-discovery rate cutoff. Purple, phosphosites conforming to the Phactr1/PP1 substrate motif S/T-$x_{2,3}$-Φ-L. Red, Phactr1/PP1 substrates identified previously (Fedoryshchak et al., 2020).

D. Enrichment of hits conforming to the Phactr1 substrate motif S/T-$x_{2,3}$-Φ-L and of hits identified in the previous study in all Phactr samples calculated using Fisher's exact test.

E. Venn diagram showing overlap between hits identified as potential Phactr1-4 substrates.

Figure 2-S1.

A. Phosphorylation sites depleted in PP1-expressing samples compared with control empty-vector samples. Dashed line, 1% false-discovery rate cutoff.

B. Frequency plots for residues identified as PP1 hits in (A) and for all phosphorylation sites in the analysis. Enrichment is broadly consistent with published findings (Hoermann et al., 2020).

C. The top Phactr1/PP1 substrate sites previously identified in mouse NIH3T3 cells (Fedoryshchak et al., 2020) are listed, and compared with the candidate substrates for the four PP1-Phactr fusions identified here in human 293 Flp-In T-Rex cells. Phosphorylation sites that could not be identified or that were not detectable in 293 Flp-In T-Rex cells are indicated. "**+**" and "**no**" indicate phosphorylation sites identified in 293 Flp-In T-Rex cells that were either sensitive (**+**) or insensitive (**no**) to PP1-Phactr fusion expression.

D-F. Specific phosphorylation site depletion in cells expressing PP1-Phactr2 (**C**), PP1-Phactr3 (**D**) or PP1-Phactr4 (**E**) fusion proteins as opposed to PP1 alone. Abundances of specific phosphorylation sites in PP1 and the different PP1-Phactr fusion samples were determined, log-transformed, and expressed as Z-scores. For each phosphorylation site, depletion in cells expressing each fusion as opposed to PP1 alone was quantified as the difference between the PP1 and PP1-Phactr fusion Z-scores, and plotted versus $-\log_{10}P$. Dashed line, 5% false-discovery rate cutoff. Purple, phosphorylation sites conforming to the Phactr1/PP1 substrate motif S/T-$x_{2,3}$-Φ-L. Red, top Phactr1/PP1 hits identified previously (Fedoryshchak et al., 2020).

Figure 2-S2

A. Identification of PP1-R15A substrates. Abundances of specific phosphorylation sites in PP1-R15A samples were determined, log-transformed, and expressed as Z-scores. For each phosphorylation site the average abundance in the remaining datasets, excluding PP1-R15B, was quantified in the same way. Depletion of phosphorylation sites in cells expressing PP1-R15A was quantified as the difference between the PP1-R15A and the dataset average Z-scores, and plotted versus $-\log_{10}P$. Dashed line, 5% false-discovery threshold.

B. Identification of PP1-R15B substrates. Depletion of each phosphorylation site in cells expressing PP1-R15B, relative to its average abundance in the other datasets, excluding PP1-R15A, was quantified and plotted as in (A). Significantly depleted phosphorylation sites are highlighted in red.

C. Identification of PP1-PNUTS substrates. Depletion of each phosphorylation site in cells expressing PP1-PNUTS, relative to its average abundance in all the other

datasets was quantified and plotted as in (A). Significantly depleted phosphorylation sites are highlighted in red. PNUTS phosphorylation sites exhibiting increased abundance, presumably reflecting PP1-PNUTS fusion expression, are highlighted in blue.

Figure 3. Phosphoproteomics of PP1-Neurabin and PP1-Spinophilin.

A. Identification of PP1-Neurabin substrates. Abundances of specific phosphorylation sites in PP1-Neurabin samples were determined, log-transformed, and expressed as Z-scores. For each phosphosite the abundance in the remaining datasets, excluding PP1-Spinophilin, was quantified in the same way. Depletion of phosphosites in cells expressing PP1-Neurabin was quantified as the difference between the PP1-Neurabin and the dataset average Z-scores, and plotted versus -$\log_{10}$P. Dashed line, 5% false-discovery threshold; significantly depleted phosphosites are highlighted in red.

B. Identification of PP1-Spinophilin substrates. Depletion of each phosphorylation site in cells expressing PP1-Spinophilin, relative to its average abundance in the other datasets, excluding PP1-Neurabin, was quantified and plotted as in (A).

C. Sequences of significantly depleted phosphorylation sites identified in **A** and **B**.

D. Immunoblot analysis of 4E-BP1 phosphorylation sites in 293 Flp-In T-Rex cells upon induced expression of PP1-Neurabin or empty vector. Note that the low level of PP1-Neurabin expression in uninduced cells (see Figure 3-S1C) alters the relative abundance of the different phosphorylated forms compared with 293 Flp-In T-Rex cells expressing vector alone.

E. Protein synthesis quantification assay. 293 Flp-In T-Rex cells expressing vector alone, PP1-Neurabin, or PP1, were induced with tetracycline (50 nM) and/or treated with rapamycin (50 nM) for 16h as indicated before treatment with *O*-propargyl puromycin to label nascent polypeptides, which were conjugated to AlexaFluor-488 azide and quantified by flow cytometry. Fluorescence intensities were normalized to untreated cells.

Figure 3-S1.

A. 4E-BP1 and 4E-BP2 levels are unaffected by PP1-Neurabin expression. Protein abundances in PP1-Neurabin cells before and after induction of PP1-Neurabin expression were determined, log-transformed, and normalized to median. Change in relative abundance upon induction was scored as the difference between the induced and uninduced samples, plotted versus $-\log_{10}P$. Dashed line, 5% false-discovery threshold. Neurabin and the 4E-BPs are highlighted in red.

B. Specificity analysis of the commercial anti-phospho-S65 antibody.

C. Basal expression of PP1-Neurabin in uninduced 293 Flp-In T-Rex cells. Data are contrast-enhanced blots from Figure 3D.

D. mTORC1 pathway schematic (see (Hoeffer and Klann, 2010; Liu and Sabatini, 2020)).

Figure 4. 4E-BP1 is a substrate of PP1-Neurabin.

A. mCherry-tagged wild-type 4E-BP1 or 4E-BP1(118+A) were expressed and purified from 293 cells, incubated with increasing amounts of recombinant

PP1-Neurabin. Phosphorylation of the indicated sites was analysed by immunoblotting.

B. Quantification of **A**.

C. Left, sequence alignment of potential Neurabin/Spinophilin PDZ domain ligands. Grey shading, hydrophobic residues; pink, acidic residues; cyan, basic residues; orange, hydrophilic residues. Underlining shows sequences N-terminally linked to 6-carboxyfluorescein (FAM) for use in fluorescence polarisation (FP) assay. Right, binding affinities for the Neurabin and Spinophilin PDZ domains as determined in the FP assay.

D. FP assay. FAM-labelled peptides (see C) were titrated with increasing concentrations of recombinant Neurabin PDZ domain and affinity estimated from change in fluorescence anisotropy. For Spinophilin data see Figure S4B.

Figure 4-S1.

A. Immunoblotting analysis of wildtype mCherry-4E-BP1 or mutants either lacking the 6 C-terminal residues (ΔCter), or containing an additional C-terminal alanine (118+A) upon expression in 293 cells with or without PP1-Neurabin expression as indicated.

B. Left, sequence alignment of potential Neurabin/Spinophilin PDZ domain ligands. Grey shading, hydrophobic residues; pink, acidic residues; cyan, basic residues; orange, hydrophilic residues. Underlining shows sequences N-terminally linked to 6-carboxyfluorescein (FAM) for use in fluorescence polarisation (FP) assay. FAM-labelled peptides were titrated with increasing concentrations of recombinant

Spinophilin PDZ domain and affinity estimated from change in fluorescence anisotropy (for summary see Figure 4C).

C. Immunoblotting analysis of S6K phosphorylation 293 Flp-In T-Rex cells upon expression of PP1-Neurabin or empty vector.

Figure 5. Substrate specificity determinants of PP1-Neurabin.

A. Top, synthetic substrate peptides contain either the 4E-BP1 T70 or IRSp53 S455 phosphorylation sites, joined by a GSG linker to the Neurabin PDZ-binding C-terminal sequences. PBM, PDZ-binding motif (FEMDI); MUT, mutated PBM (FE**sgs**). Below, sequences of the different peptides analysed; highlights indicate the dephosphorylation site (yellow), the +4/+6 region (orange), and the PDZ-binding sequence (cyan), with alanine and other substitutions indicated in red. Peptides were treated with recombinant PP1-Neurabin, PP1-Phactr1 or PP1 in the presence of the phosphate sensor, and K_M and catalytic efficiencies determined. K_M are shown at the right; for catalytic efficiency quantification see Figure 5-S1A. For raw and processed data, see Supplementary Table 3.

B-E. Panels show relative catalytic efficiencies as determined from data displayed in Figure 5-S1B-E. Each panel shows different subsets of the data to highlight comparison between different enzymes and/or substrates. For raw and processed data, see Supplementary Table 3. **B.** Comparison of Neurabin-PP1 and Phactr1-PP1 substrates 4E-BP1 and IRSp53 to assess the role of the Neurabin PDZ domain in substrate recognition. **C.** Role of the +4/+6 region in 4E-BP1 substrate recognition. **D.** Role of the +5 residue in IRSp53 substrate recognition. **E.** Role of 4E-BP1 +1/+2 residues.

Figure 5-S1.

A. Catalytic efficiencies for the various peptide dephosphorylation reactions by PP1-Neurabin, PP1-Phactr1 and PP1 are shown. For raw and processed data, see Supplementary Table 3.

B-E. Dephosphorylation reaction rates plotted against substrate concentration for different sets of phosphopeptides with PP1-Neurabin, PP1-Phactr1 or PP1.

Figure 5-S2

Schematic showing the mechanisms of substrate binding by Phactr1/PP1 and Neurabin/PP1 complexes. Phosphate groups are indicated by red lollipops, the Phactr1 consensus in orange, and the Neurabin PBM motif in cyan.

Figure 6. Structural analysis of 4E-BP1 interactions with PP1-Neurabin.

A. Schematic of the PP1-4E-BP1 chimera and of Neurabin PP1-interacting and PDZ domain sequences.

B. Crystal structure of the PP1-4E-BP1/Neurabin complex. PP1 in white surface representation, Neurabin in lilac surface representation, 4E-BP1 in blue stick representation, with unresolved sequences indicated by dashed line. PP1 active site presumptive Mn^{2+} ions in purple.

C. Comparison of PP1-4E-BP1/Neurabin complex structure with the previously published Neurabin/PP1 holophosphatase structure (9PDB 3HVQ)(Ragusa et al., 2010). PP1 in white surface representation, Neurabin in ribbon representation (lilac,

PP1-4E-BP1/Neurabin; red, Neurabin/PP1). 4E-BP1 in blue stick representation, unresolved sequences not shown. Structures are superimposed on PP1 residues 7-298 (rmsd=0.21 Å, 277 alpha carbons).

D. Close-up view of interactions between 4E-BP1 C-terminal sequences (blue sticks) with the Neurabin PDZ domain (lilac cartoons).

E. AlphaFold3 model of the phosphorylated PP1-4E-BP1 chimera / Neurabin(423-593) interaction. A close-up view of predicted interaction of pT70 with the PP1 catalytic site is shown. For PAE and pLDDT plots, see Figure 6-S2A. PP1 and Neurabin are shown respectively in white and lilac surface representation, with PP1 active site Mn^{2+} ions in purple. 4E-BP1 sequences are in stick representation, colour-coded according to the AlphaFold3 pLDDT score (inset). See also Figure 6-S2C.

F. AlphaFold3 modelling of the Neurabin(423-593)/PP1 - 5x phospho-4E-BP1 interaction. PP1 and Neurabin are shown respectively in white and lilac surface representation, with PP1 active site Mn^{2+} ions in purple. 4E-BP1 sequences are in ribbon and stick representation, colour-coded according to the AlphaFold3 pLDDT score (inset), with the 4E-BP1 phosphorylations at T37, T46, S65, T70 and S101 shown in spheres. For PAE and pLDDT plots, see Figure 6-S2F.

Figure 6-S1.

A. Crystal structure of the PP1-4E-BP1/Neurabin complex. PP1 in white surface representation, with active site presumptive Mn^{2+} ions in purple, Neurabin in lilac cartoon representation, and 4E-BP1 in blue stick representation. PP1 2Fo-Fc electronic density contoured at 1 sigma level is displayed around Neurabin.

B. Comparison of the PBM-liganded Neurabin PDZ domain (pink ribbons) with the previously published structure of the unliganded Neurabin PDZ domain (red ribbons) (PDB 3HVQ,Ragusa et al., 2010). The 4E-BP1 PBM is shown in blue stick representation.

Figure 6-S2.

A, B. AlphaFold3 models of the phosphorylated **(A)** and unphosphorylated **(B)** PP1-4E-BP1 chimera / Neurabin(423-593) interaction. Left, PAE plots; right, pLDDT plots, with confidence boundaries indicated by dashed lines (>90%, very high (side-chains); 70-90%, high (main-chain); 50-70%, low).

C, D. AlphaFold3 models of the phosphorylated **(C)** and unphosphorylated **(D)** PP1-4E-BP1 chimera / Neurabin(423-593) interaction. PP1 and Neurabin are shown respectively in white and lilac surface representation with PP1 active site Mn^{2+} ions in purple. 4E-BP1 sequences are in stick representation, colour coded according to the AlphaFold3 pLDDT score (inset), with pT70 and T70 in space-fill; linker residues are in black. Below are shown close-up views of predicted interactions with the PP1 catalytic site. For PAE and pLDDT plots, see **A, B**.

E. Comparison of crystal structure and AlphaFold3 model of 4E-BP1/PDZ interactions in phosphorylated and unphosphorylated PP1-4E-BP1 chimera / Neurabin(423-593) interaction. Predicted structures are oriented by superposition of the PDZ domain, shown in lilac ribbon representation. 4E-BP1 sequences are in stick representation, colour coded according to the AlphaFold3 pLDDT score as in panels C,D. Note that AlphaFold3 does not predict any interaction between the

Neurabin PDZ domain and the 4E-BP1(118+A) PBM mutant characterised in Figure 4.

F. AlphaFold3 modelling of the Neurabin(423-593)/PP1 - 5x phospho-4E-BP1 interaction. Left, PAE plots; right, pLDDT plots, with confidence boundaries indicated by dashed lines (>90%, very high (side-chains); 70-90%, high (main-chain); 50-70%, low).

REFERENCES

Abramson J, Adler J, Dunger J, Evans R, Green T, Pritzel A, Ronneberger O, Willmore L, Ballard AJ, Bambrick J *et al* (2024) **Accurate structure prediction of biomolecular interactions with AlphaFold 3**. *Nature* **630**: 493-500

Adams PD, Afonine PV, Bunkoczi G, Chen VB, Davis IW, Echols N, Headd JJ, Hung LW, Kapral GJ, Grosse-Kunstleve RW *et al* (2010) **PHENIX: a comprehensive Python-based system for macromolecular structure solution**. *Acta Crystallogr D Biol Crystallogr* **66**: 213-221

Aguilar-Valles A, Matta-Camacho E, Khoutorsky A, Gkogkas C, Nader K, Lacaille JC, Sonenberg N (2015) **Inhibition of Group I Metabotropic Glutamate Receptors Reverses Autistic-Like Phenotypes Caused by Deficiency of the Translation Repressor eIF4E Binding Protein 2**. *J Neurosci* **35**: 11125-11132

Allen PB, Ouimet CC, Greengard P (1997) **Spinophilin, a novel protein phosphatase 1 binding protein localized to dendritic spines**. *Proc Natl Acad Sci U S A* **94**: 9956-9961

Artemenko M, Zhong SSW, To SKY, Wong AST (2022) **p70 S6 kinase as a therapeutic target in cancers: More than just an mTOR effector**. *Cancer Lett* **535**: 215593

Bollen M, Peti W, Ragusa MJ, Beullens M (2010) **The extended PP1 toolkit: designed to create specificity**. *Trends Biochem Sci* **35**: 450-458

Brautigan DL, Shenolikar S (2018) **Protein Serine/Threonine Phosphatases: Keys to Unlocking Regulators and Substrates**. *Annu Rev Biochem* **87**: 921-964

Burnett PE, Blackshaw S, Lai MM, Qureshi IA, Burnett AF, Sabatini DM, Snyder SH (1998) **Neurabin is a synaptic protein linking p70 S6 kinase and the neuronal cytoskeleton**. *Proc Natl Acad Sci U S A* **95**: 8351-8356

Casamayor A, Arino J (2020) **Controlling Ser/Thr protein phosphatase PP1 activity and function through interaction with regulatory subunits**. *Adv Protein Chem Struct Biol* **122**: 231-288

Cenik BK, Shilatifard A (2021) **COMPASS and SWI/SNF complexes in development and disease**. *Nat Rev Genet* **22**: 38-58

Chen R, Rato C, Yan Y, Crespillo-Casado A, Clarke HJ, Harding HP, Marciniak SJ, Read RJ, Ron D (2015) **G-actin provides substrate-specificity to eukaryotic initiation factor 2alpha holophosphatases**. *Elife* **4**

Choy MS, Hieke M, Kumar GS, Lewis GR, Gonzalez-DeWhitt KR, Kessler RP, Stein BJ, Hessenberger M, Nairn AC, Peti W *et al* (2014) **Understanding the antagonism of retinoblastoma protein dephosphorylation by PNUTS provides insights into the PP1 regulatory code**. *Proc Natl Acad Sci U S A* **111**: 4097-4102

Cohen PT (2002) **Protein phosphatase 1--targeted in many directions**. *J Cell Sci* **115**: 241-256

Cortazar MA, Sheridan RM, Erickson B, Fong N, Glover-Cutter K, Brannan K, Bentley DL (2019) **Control of RNA Pol II Speed by PNUTS-PP1 and Spt5 Dephosphorylation Facilitates Termination by a "Sitting Duck Torpedo" Mechanism**. *Mol Cell* **76**: 896-908 e894

Egloff MP, Cohen PT, Reinemer P, Barford D (1995) **Crystal structure of the catalytic subunit of human protein phosphatase 1 and its complex with tungstate**. *J Mol Biol* **254**: 942-959

Emsley P, Lohkamp B, Scott WG, Cowtan K (2010) **Features and development of Coot**. *Acta Crystallogr D Biol Crystallogr* **66**: 486-501

Erickson B, Fedoryshchak RO, Fong N, Sheridan RM, Larson KY, Saviola AJ, Stephane Mouilleron S, Kirk C. Hansen KC, Treisman R, Bentley DL (2024) **PP1 PNUTS binds the "restrictor" and dephosphorylates RNA pol II CTD Ser5 to stimulate transcription termination**. *Genes Dev* **submitted for publication**

Fedoryshchak RO, Prechova M, Butler AM, Lee R, O'Reilly N, Flynn HR, Snijders AP, Eder N, Ultanir S, Mouilleron S *et al* (2020) **Molecular basis for substrate specificity of the Phactr1/PP1 phosphatase holoenzyme**. *Elife* **9**

Foley K, McKee C, Nairn AC, Xia H (2021) **Regulation of Synaptic Transmission and Plasticity by Protein Phosphatase 1**. *J Neurosci* **41**: 3040-3050

Goldberg J, Huang HB, Kwon YG, Greengard P, Nairn AC, Kuriyan J (1995) **Three-dimensional structure of the catalytic subunit of protein serine/threonine phosphatase-1**. *Nature* **376**: 745-753

Harris BZ, Lim WA (2001) **Mechanism and role of PDZ domains in signaling complex assembly**. *J Cell Sci* **114**: 3219-3231

Hoeffer CA, Klann E (2010) **mTOR signaling: at the crossroads of plasticity, memory and disease**. *Trends Neurosci* **33**: 67-75

Hoermann B, Kokot T, Helm D, Heinzlmeir S, Chojnacki JE, Schubert T, Ludwig C, Berteotti A, Kurzawa N, Kuster B *et al* (2020) **Dissecting the sequence determinants for dephosphorylation by the catalytic subunits of phosphatases PP1 and PP2A**. *Nat Commun* **11**: 3583

Holt CE, Martin KC, Schuman EM (2019) **Local translation in neurons: visualization and function**. *Nat Struct Mol Biol* **26**: 557-566

Jones AW, Flynn HR, Uhlmann F, Snijders AP, Touati SA (2020) **Assessing Budding Yeast Phosphoproteome Dynamics in a Time-Resolved Manner using TMT10plex Mass Tag Labeling**. *STAR Protoc* **1**: 100022

Kelker MS, Dancheck B, Ju T, Kessler RP, Hudak J, Nairn AC, Peti W (2007) **Structural basis for spinophilin-neurabin receptor interaction**. *Biochemistry* **46**: 2333-2344

Lee JH, You J, Dobrota E, Skalnik DG (2010) **Identification and characterization of a novel human PP1 phosphatase complex**. *J Biol Chem* **285**: 24466-24476

Liu GY, Sabatini DM (2020) **mTOR at the nexus of nutrition, growth, ageing and disease**. *Nat Rev Mol Cell Biol* **21**: 183-203

Liu J, Stevens PD, Eshleman NE, Gao T (2013) **Protein phosphatase PPM1G regulates protein translation and cell growth by dephosphorylating 4E binding protein 1 (4E-BP1)**. *J Biol Chem* **288**: 23225-23233

Martineau Y, Azar R, Bousquet C, Pyronnet S (2013) **Anti-oncogenic potential of the eIF4E-binding proteins**. *Oncogene* **32**: 671-677

McCoy AJ, Grosse-Kunstleve RW, Adams PD, Winn MD, Storoni LC, Read RJ (2007) **Phaser crystallographic software**. *J Appl Crystallogr* **40**: 658-674

Novoa I, Zeng H, Harding HP, Ron D (2001) **Feedback inhibition of the unfolded protein response by GADD34-mediated dephosphorylation of eIF2alpha**. *J Cell Biol* **153**: 1011-1022

Penzes P, Johnson RC, Sattler R, Zhang X, Huganir RL, Kambampati V, Mains RE, Eipper BA (2001) **The neuronal Rho-GEF Kalirin-7 interacts with PDZ domain-containing proteins and regulates dendritic morphogenesis**. *Neuron* **29**: 229-242

Ragusa MJ, Dancheck B, Critton DA, Nairn AC, Page R, Peti W (2010) **Spinophilin directs protein phosphatase 1 specificity by blocking substrate binding sites**. *Nat Struct Mol Biol* **17**: 459-464

Romagnoli A, D'Agostino M, Ardiccioni C, Maracci C, Motta S, La Teana A, Di Marino D (2021) **Control of the eIF4E activity: structural insights and pharmacological implications**. *Cell Mol Life Sci* **78**: 6869-6885

Sarrouilhe D, di Tommaso A, Metaye T, Ladeveze V (2006) **Spinophilin: from partners to functions**. *Biochimie* **88**: 1099-1113

Schalm SS, Blenis J (2002) **Identification of a conserved motif required for mTOR signaling**. *Curr Biol* **12**: 632-639

Subbaiah VK, Kranjec C, Thomas M, Banks L (2011) **PDZ domains: the building blocks regulating tumorigenesis**. *Biochem J* **439**: 195-205

Tonikian R, Zhang Y, Sazinsky SL, Currell B, Yeh JH, Reva B, Held HA, Appleton BA, Evangelista M, Wu Y *et al* (2008) **A specificity map for the PDZ domain family**. *PLoS Biol* **6**: e239

Tyanova S, Temu T, Sinitcyn P, Carlson A, Hein MY, Geiger T, Mann M, Cox J (2016) **The Perseus computational platform for comprehensive analysis of (prote)omics data**. *Nat Methods* **13**: 731-740

Vaguine AA, Richelle J, Wodak SJ (1999) **SFCHECK: a unified set of procedures for evaluating the quality of macromolecular structure-factor data and their agreement with the atomic model**. *Acta Crystallogr D Biol Crystallogr* **55**: 191-205

Ward RJ, Alvarez-Curto E, Milligan G (2011) **Using the Flp-In T-Rex system to regulate GPCR expression**. *Methods Mol Biol* **746**: 21-37

Winter G, Lobley CM, Prince SM (2013) **Decision making in xia2**. *Acta Crystallogr D Biol Crystallogr* **69**: 1260-1273

Wu LJ, Ren M, Wang H, Kim SS, Cao X, Zhuo M (2008) **Neurabin contributes to hippocampal long-term potentiation and contextual fear memory**. *PLoS One* **3**: e1407

Yan Y, Harding HP, Ron D (2021) **Higher-order phosphatase-substrate contacts terminate the integrated stress response**. *Nat Struct Mol Biol* **28**: 835-846

Yan Z, Hsieh-Wilson L, Feng J, Tomizawa K, Allen PB, Fienberg AA, Nairn AC, Greengard P (1999) **Protein phosphatase 1 modulation of neostriatal AMPA channels: regulation by DARPP-32 and spinophilin**. *Nat Neurosci* **2**: 13-17

Yang H, Jiang X, Li B, Yang HJ, Miller M, Yang A, Dhar A, Pavletich NP (2017) **Mechanisms of mTORC1 activation by RHEB and inhibition by PRAS40**. *Nature* **552**: 368-373

Figure 1

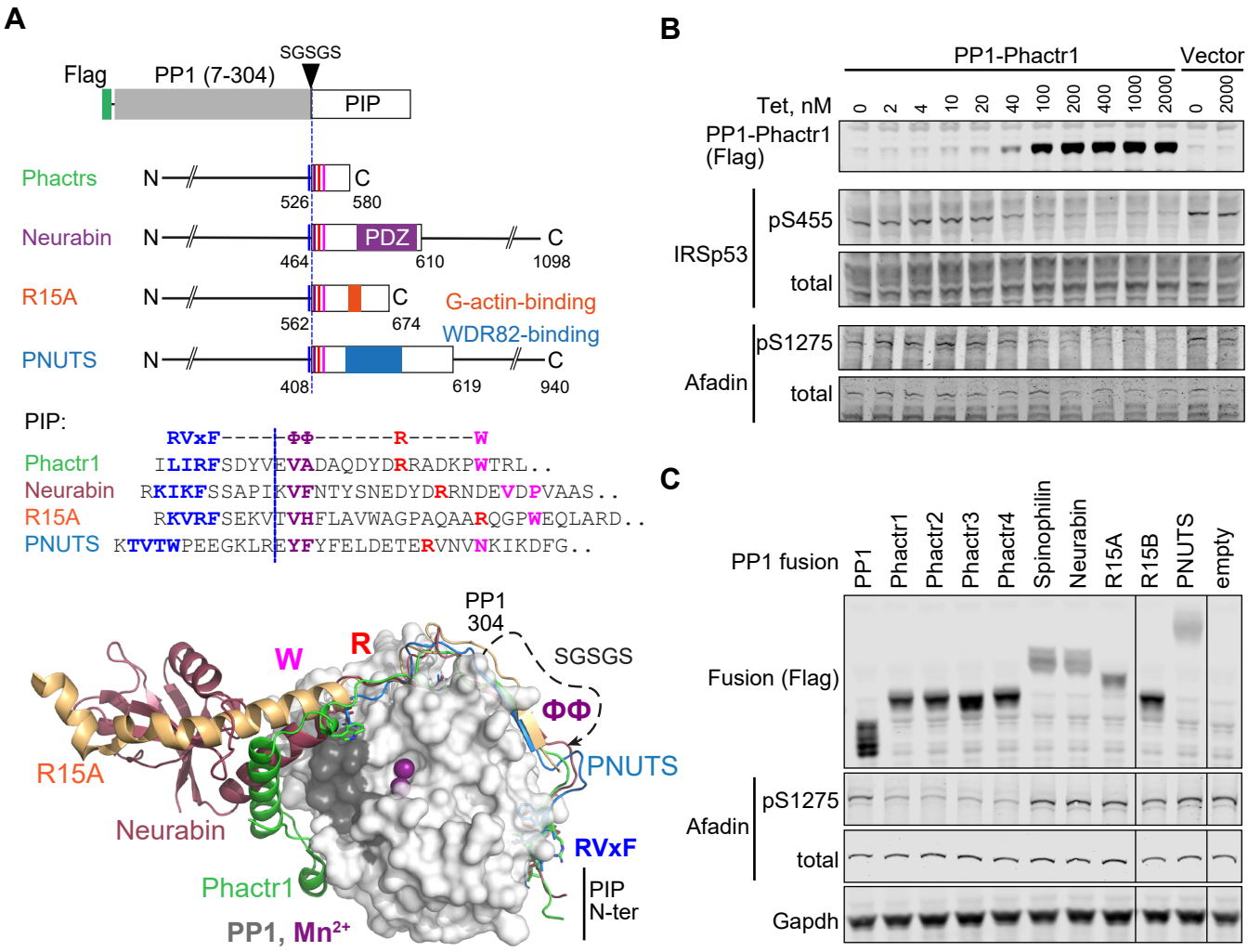
A
Flag
PP1 (7-304)
SGSGS
PIP
Phactrs
N
C
526
580
Neurabin
PDZ
464
610
1098
R15A
562
674
G-actin-binding
WDR82-binding
PNUTS
408
619
940
PIP:
RVxF
ΦΦ
R
W
Phactr1 ILIRFSDYVEVADAQDYDRRADKPWTRL..
Neurabin RKIKFSSAPIKVFNTYSNEDYDRRNDEVDPVAAS..
R15A RKVRFSEKVTVHFLAVWAGPAQAARQGPWEQLARD..
PNUTS KTVTWPEEGKLREYFYFELDETERVNVNKIKDFG..
PP1
304
SGSGS
ΦΦ
PNUTS
R15A
Neurabin
Phactr1
RVxF
PIP
N-ter
PP1, Mn2+
B
PP1-Phactr1
Vector
Tet, nM
0
2
4
10
20
40
100
200
400
1000
2000
0
2000
PP1-Phactr1
(Flag)
IRSp53
pS455
total
Afadin
pS1275
total
C
PP1 fusion
PP1
Phactr1
Phactr2
Phactr3
Phactr4
Spinophilin
Neurabin
R15A
R15B
PNUTS
empty
Fusion (Flag)
Afadin
pS1275
total
Gapdh

Figure 1-S1.

A

```
                 RVxF     ΦΦ      R     W      Substrate-determining region
Phactr1   514  RERKILIRFSDYVEVADAQDYDRRADKPWTRLTAADKAAIRKELNEFKSTEMEVHELSRHLTRFHRP  580 (C-term)
Phactr2   569  QARR-ILRFNEYVEVTDSPDYDRRADKPWARLTPADKAAIRKELNEFKSTEMEVHEESRQFTRFHRP  634 (C-term)
Phactr3   493  RDRKILIRFSDYVEVAKAQDYDRRADKPWTRLSAADKAAIRKELNEYKSNEMEVHASSKHLTRFHRP  559 (C-term)
Phactr4   637  LARK-ILRFNEYVEVTDAQDYDRRADKPWTKLTPADKAAIRKELNEFKSSEMEVHEESKHFTRYHRP  702 (C-term)
                 *: ::**.:****:.: **********::*: *************:**.*****  *:::**:***

                 RVxF     ΦΦ          R     W                    PDZ domain
Neurabin  451  IPANRKIKFSSAPIKVFNTYSNEDYDRRNDEVDPVAASAEYELEKRVEKLELFPVELEKDEDGLGISIIGMGVGADAGL  529
Spinophilin 443 PAPSRKIHFSTAPIQVFSTYSNEDYDRRNEDVDPMAASAEYELEKRVERLELFPVELEKDSEGLGISIIGMGAGADMGL  521
                  .***:**:***:**.***********::***:**************:***********.:**********.*** **

                                PDZ domain
Neurabin  530  EKLGIFVKTVTEGGAAQRDGRIQVNDQIVEVDGISLVGVTQNFAATVLRNTKGNVRFVIGREKPGQV  596
Spinophilin 522 EKLGIFVKTVTEGGAAHRDGRIQVNDLLVEVDGTSLVGVTQSFAASVLRNTKGRVRFMIGRERPGEQ  588
                ****************:********* :***** *******.***:*******.***:****:**:

                 RVxF     ΦΦ          R    W   G-actin binding helix
R15A      549  PLKARKVRFSEKVTVHFLAVWAGPAQAARQGPWEQLARDRSRFARRITQAQEELSPCLTPAARARAWARLRNPPLAPIPALTQT  633
R15B      634  HVKRKKVTFLEEVTEYYI-----SGDEDRKGPWEEFARDGCRFQKRIQETEDAIGYCLTFEHRERMFNRLQGTCFKGLNVLKQC  713 (C-term)
                :* :** * *:** :::       .:  *:****::*** .** :** :::: :. ***   * * : **:.  :  : .*.*

R15A      634  LPSSSVPSSPVQTTPLSQAVATPSRSSAAAAAALDLSGRRG  674 (C-term)

                 RVxF     ΦΦ          R    W                    WDR82-binding
PNUTS     393  GRKRKSVTWPEEGKLREYFYFELDETERVNVNKIKDFGEAAKREILSDRHAFETARRLSHDNMEEKVPWVCPRPLVLPSPLVTP  476

                                WDR82-binding
PNUTS     477  GSNSQERYIQAEREKGILQELFLNKESPHEPDPEPYEPIPPKLIPLDEECSMDETPYVETLEPGGSGGSPDGAGGSKLPPVLAN  560

PNUTS     561  LMGSMGAGKGPQGPGGGGINVQEILTSIMGSPNSHPSEELLKQPDYSDKIKQMLVPHGL  619
```

B

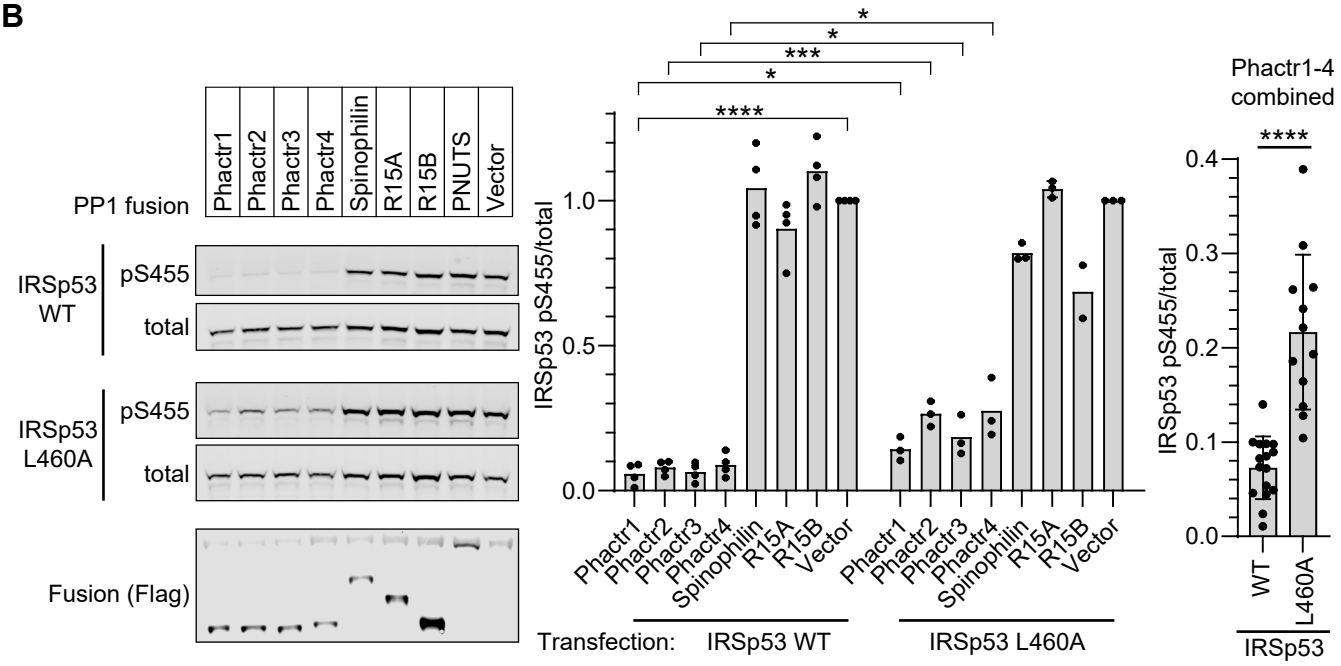

Figure 1-S2.

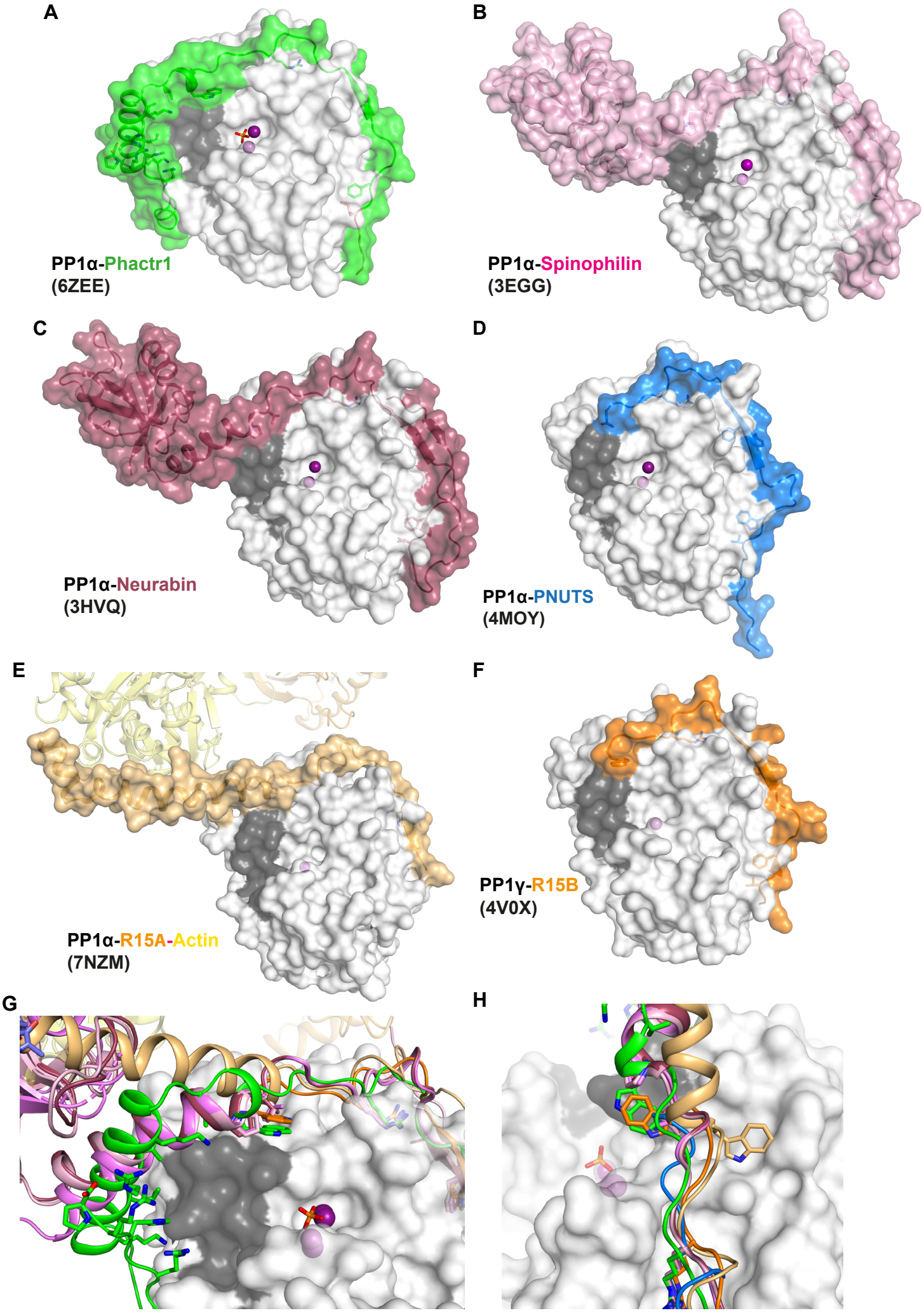
A
PP1α-Phactr1
(6ZEE)
B
PP1α-Spinophilin
(3EGG)
C
PP1α-Neurabin
(3HVQ)
D
PP1α-PNUTS
(4MOY)
E
PP1α-R15A-Actin
(7NZM)
F
PP1γ-R15B
(4V0X)
G
H

Figure 2

A

Induction of fusions expression with tetracycline → Lysis and protease digestion → TMT labelling → Phosphopeptide enrichment on FeNTA beads → Phosphopeptide enrichment on TiO_2 beads → Mass-spectrometry → 15620 phospho-peptides /3697 proteins

B

	Empty	PP1	Phactr1	Phactr2	Phactr3	Phactr4	PNUTS	R15A	R15B	Neurabin	Spin.
Empty	0.58										
PP1	-0.19	0.58									
Phactr1	-0.44	-0.07	0.83								
Phactr2	-0.33	-0.13	0.76	0.83							
Phactr3	-0.32	-0.16	0.76	0.82	0.83						
Phactr4	-0.23	-0.10	0.66	0.78	0.77	0.81					
PNUTS	0.20	0.00	-0.28	-0.30	-0.26	-0.30	0.39				
R15A	0.49	-0.14	-0.39	-0.30	-0.28	-0.18	0.19	0.52			
R15B	0.31	-0.06	-0.36	-0.36	-0.29	-0.32	0.24	0.23	0.48		
Neurabin	0.11	0.14	-0.27	-0.36	-0.34	-0.40	0.28	0.02	0.22	0.50	
Spinophilin	-0.07	0.22	-0.09	-0.23	-0.22	-0.24	0.15	-0.06	0.04	0.33	0.33

Pearson's correlation: 0.8 – 0

C

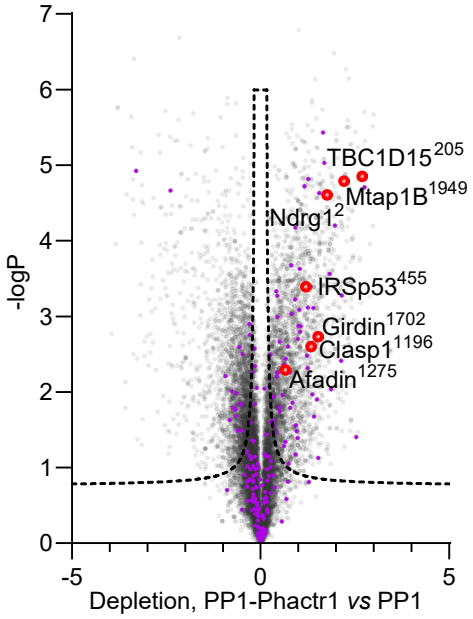

D

Phactr1/PP1 substrate motif S/T-$x_{2,3}$-Φ-L

	Enrichment factor	-logP
Phactr1	1.6	4.6
Phactr2	1.5	3.9
Phactr3	1.5	3.7
Phactr4	1.7	6.6
in common	2.0	6.5

Phactr1/PP1 substrates (Fedoryshchak et al 2020)

	Enrichment factor	-logP
Phactr1	3.6	6.4
Phactr2	3.3	5.4
Phactr3	3.4	6.1
Phactr4	3.3	5.4
in common	5.5	8.2

E

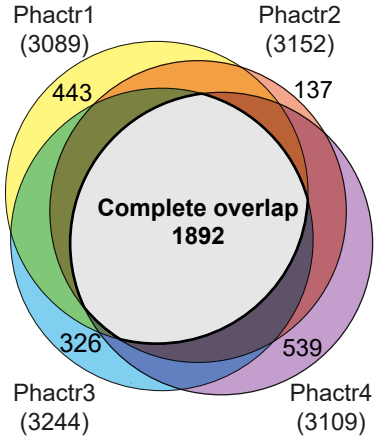

Figure 2 S1

A

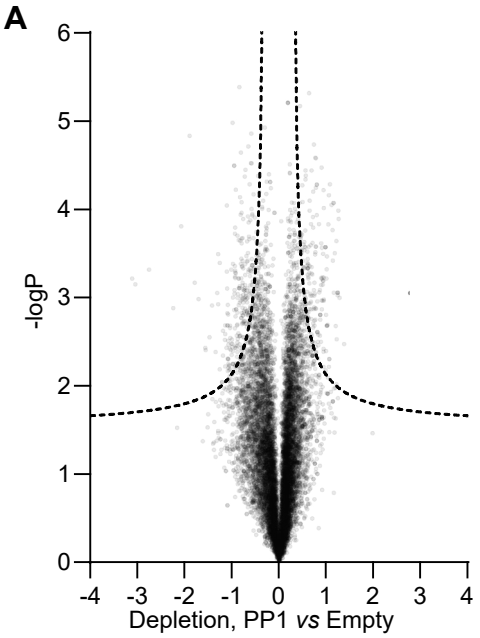

B

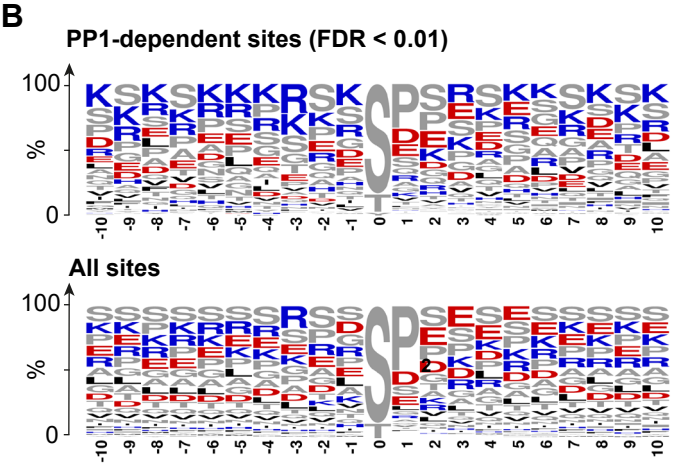

C

Phactr1 hits in mouse 3T3*			homologous human sites		PP1 fusion hit in human HEK293?				phosphorylation site sequence (mouse/human)																			
Gene	Amino acid	Position	Amino acid	Position	Phactr1	Phactr2	Phactr3	Phactr4	-8	-7	-6	-5	-4	-3	-2	-1	0	1	2	3	4	5	6	7	8
IRSp53	S	455	S	454	+	+	+	+	S	L	Q	Q	G	K	S	S	S	T	G	N	L	L	D	K	D
Eif4b	S	497	S	502	+	+	+	+	S	N	P	P	A	R	S	Q	S	S	D	T	E	Q	P/Q	S	P
Mtap1b	T	1945	T	1949	+	+	+	+	E	I	T/I	E	K	T	T	R	T	P	E	E	G	G	Y	S	Y
Plekho2	S	395	S	340	no	no	no	no	S/P	Q	F	H	P	R	S/C	S	S	L	G	D	L	L	R/G	E	S/G
Ndrg1	S	2	S	2	+	+	+	+	_	_	_	_	_	_	_	M	S	R	E	L/M	H/Q	D	V	D	L
Spectrin	S	1031	not identified/not seen																						
Cd2ap	S	458	S	458	+	+	+	+	E	Q	L	P	V/L	R	P	K	S	V	D	L/F	D	A/S	F/L	V/T	A/V
Clasp1	S	1194	S	1135	+	+	+	+	A	I	E	K	F	S	F	R	S	Q	E	D	L	N	E	P	I
Tpd52l2	S	189	not identified/not seen																						
Plectin	T	3889	T	3861	+	no	+	no	F	R	G	L	R	K	Q	I	T	V/M	E	E	L	V	R	S	Q
Ahnak	S	1283	not identified/not seen																						
Afadin	S	1282	S	1234	+	+	+	+	I	A	I	Q	R	V	T	R	S	Q	E	E	L	R	E	E/D	K
Layilin	S	299	not identified/not seen																						
Gapvd1	S	902	S	876	+	+	+	+	P	E	R	L	V	R	S	R	S	S	D	I	V	S	S	V	R
Pcm1	S	1729	S	1722	+	+	+	+	R/K	I/R	L/I	E/L	G/E	D	H	G	S	P	A	G	E	I	D	D	E
Ctnnd1	T	869	not identified/not seen																						
Dclk1	S	352	not identified/not seen																						
Bmp2k	S	929	not identified/not seen																						
Palladin	S	1009	not identified/not seen																						
Snx7	T	351	not identified/not seen																						
Cofilin-2	S	3	S	3	no	no	no	no	_	_	_	_	_	_	M	A	S	G	V	T	V	N	D	E	V
Cofilin-1	S	3	S	3	no	no	no	no	_	_	_	_	_	_	M	A	S	G	V	A	V	S	D	G	V
Tbc1d15	S	205	S	205	+	+	+	+	C	Q	N	K	S	L	S	Q	S	F	E	N	L	L	D	E	P
Anilin	S	653	not identified/not seen																						
Smap	S	17	S	17	+	+	+	+	P	H	G	V	K	R	S	A	S	P	D	D	D	L	G	S	S
Bud13	T	144	T	135	+	+	+	+	P/S	P	R	K/R	A/V	R	H	D/G	T	P	D	P	S	P	P/R	R/K	K/D
Girdin	S	1822	S	1702	+	+	+	+	A/T	E/S	G/V	T/Q	T/I	R/K	R/S	T/S	S	I/Q	H/E	D/N	F/L	L	S/D	K/E	D/V
Destrin	S	3	S	3	no	no	no	no	_	_	_	_	_	_	M	A	S	G	V	Q	V	A	D	E	V

* as measured in Fedoryshchak et al., eLife 2020

D

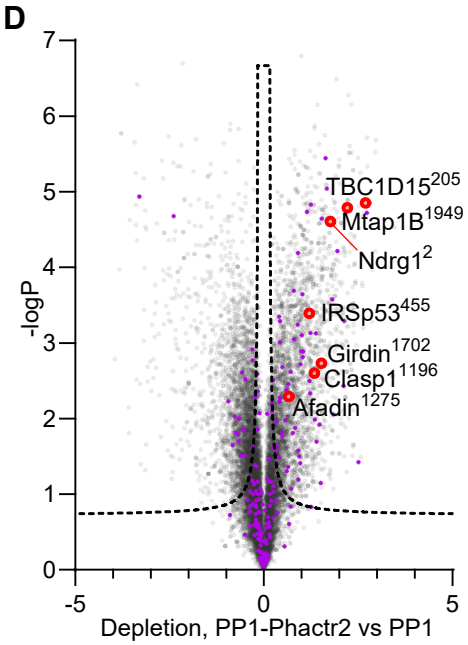

E

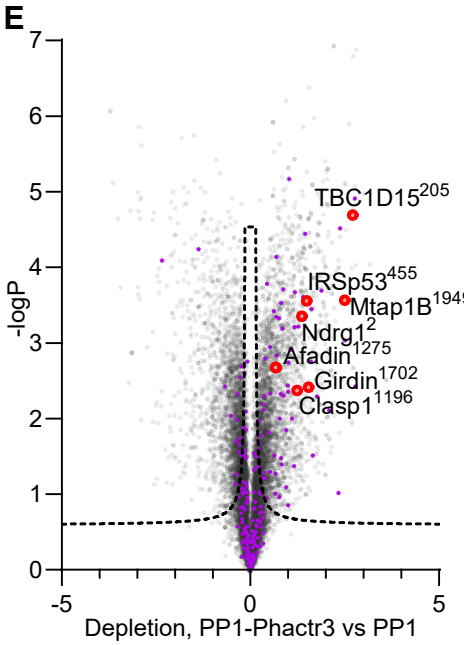

F

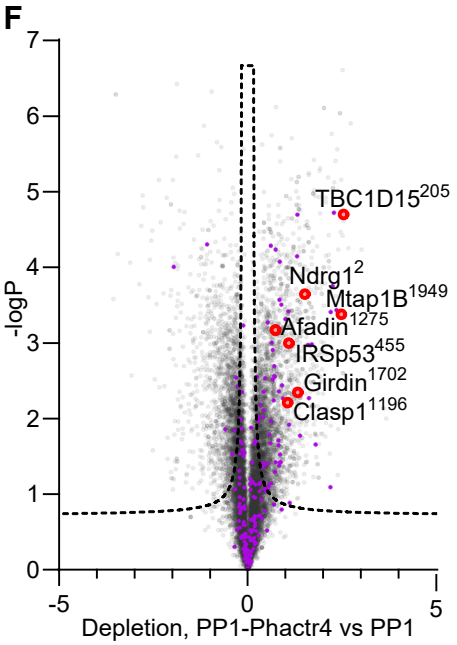

Figure 2 S2

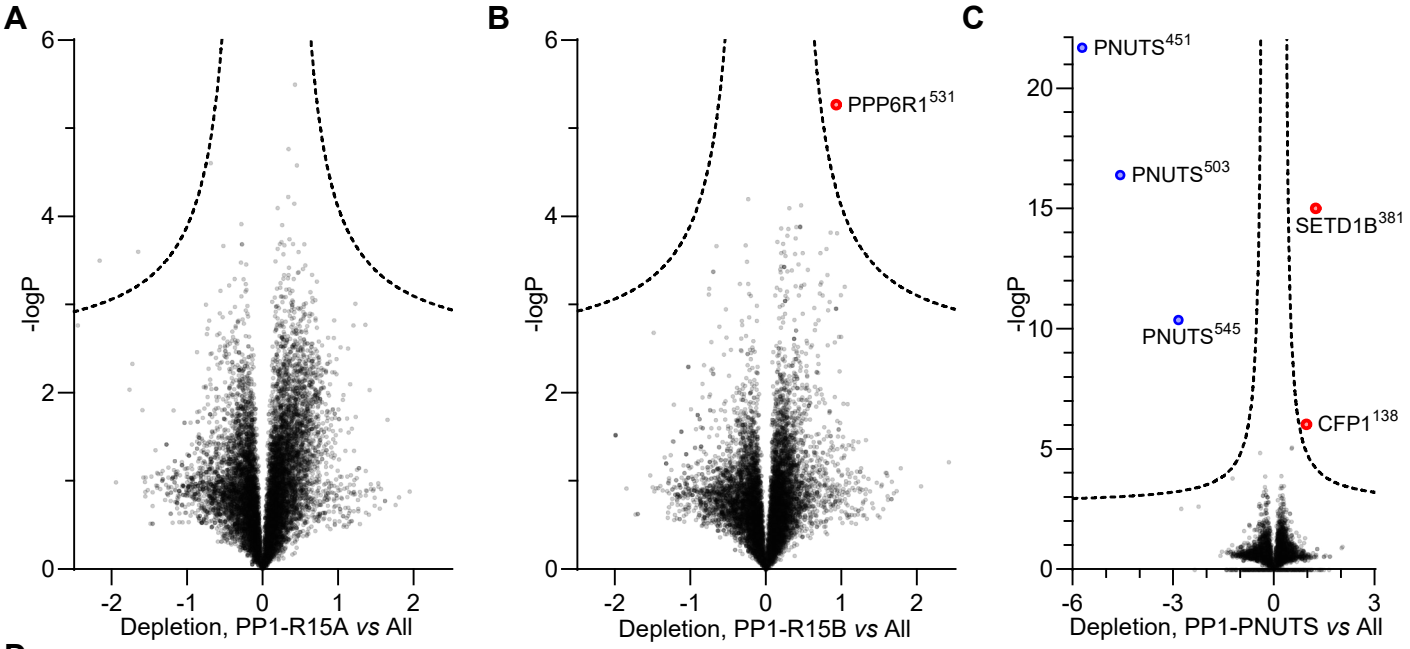

D

Protein	Site	Sequence	PP1-PNUTS Fold depl.	PP1-PNUTS -logP
CFP1	138	VGAMLARGSASPHKSSPQPLV	1.0	6.0
SETD1B	381	QPQDSATFAHTPPPAQATPAP	1.2	15.0

-10 -5 0 5 10

Figure 3

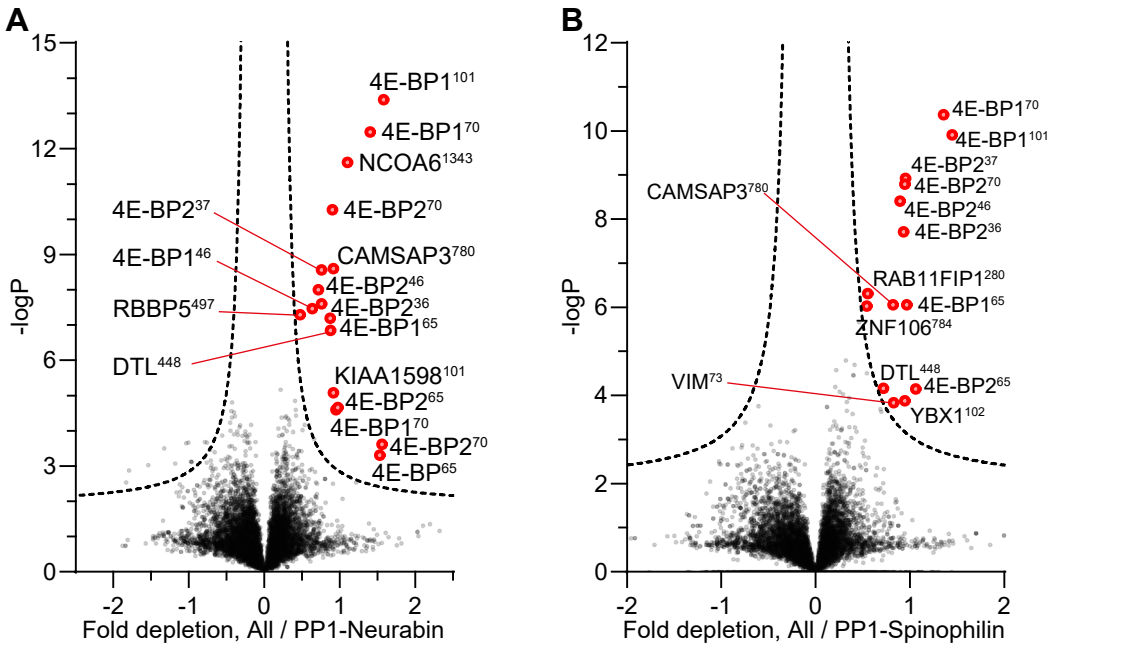

C

Protein	Site	Sequence	PP1-Neurabin Fold depl.	PP1-Neurabin -logP	PP1-Spinophilin Fold depl.	PP1-Spinophilin -logP
4E-BP2	36	DAAQLPHDYCTTPGGTLFSTT	0.8	7.6	0.9	7.7
4E-BP2	37	AAQLPHDYCTTPGGTLFSTTP	0.8	8.6	1.0	8.9
4E-BP1	46	TTPGGTLFSTTPGGTRIIYDR	0.6	7.5	0.8	n.s.
4E-BP2	46	TTPGGTLFSTTPGGTRIIYDR	0.7	8.0	0.9	8.4
4E-BP1	65	DRKFLMECRNSPVTKTPPRDL	0.9	7.2	1.0	6.1
4E-BP2	65	DRKFLLDRRNSPMAQTPPCHL	1.5	3.3	1.1	4.1
4E-BP1	70	MECRNSPVTKTPPRDLPTIPG	1.4	12.5	1.4	10.4
4E-BP2	70	LDRRNSPMAQTPPCHLPNIPG	0.9	10.3	0.9	8.8
4E-BP1	101	MEASQSHLRNSPEDKRAGGEE	1.6	13.4	1.4	9.9
DTL	448	INRRGSVSSVSPKPPSSFKMS	0.9	6.8	0.7	4.2
CAMSAP3	780	PGPGPSQSPRSPKHTRPAELR	0.9	8.6	0.8	6.1
RBBP5	497	PKGSKGKEKDSPFKPKLYKGD	0.5	7.3	0.5	n.s.
KIAA1598	101	NKENKTLKRISMLYMAKLGPD	0.9	5.1	1.1	n.s.
NCOA6	1343	SPGSSRKTTPSPGRQNSKAPK	1.1	11.6	0.5	n.s.
YBX1	102	KKNNPRKYLRSVGDGETVEFD	0.7	n.s.	0.9	3.9
VIM	73	TRSSAVRLRSSVPGVRLLQDS	0.7	n.s.	0.8	3.8
RAB11FIP1	280	SDVMSHKRTASTDLKQLNQVN	0.3	n.s.	0.6	6.3
ZNF106	784	LNSARRIRNISGHRKSETEKE	0.3	n.s.	0.5	6.0

D

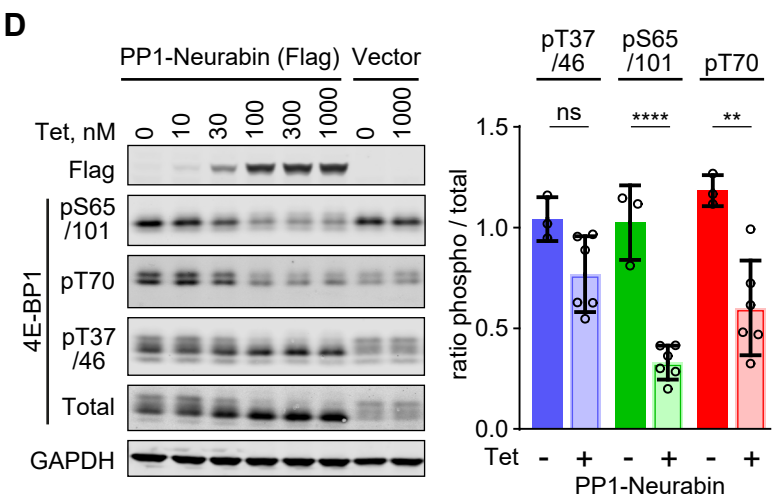

E

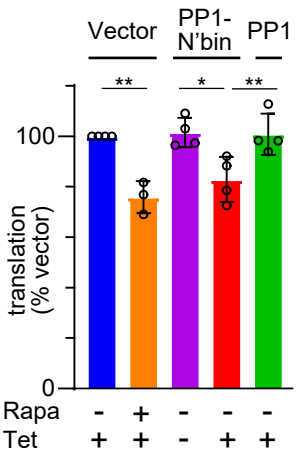

Figure 3-S1

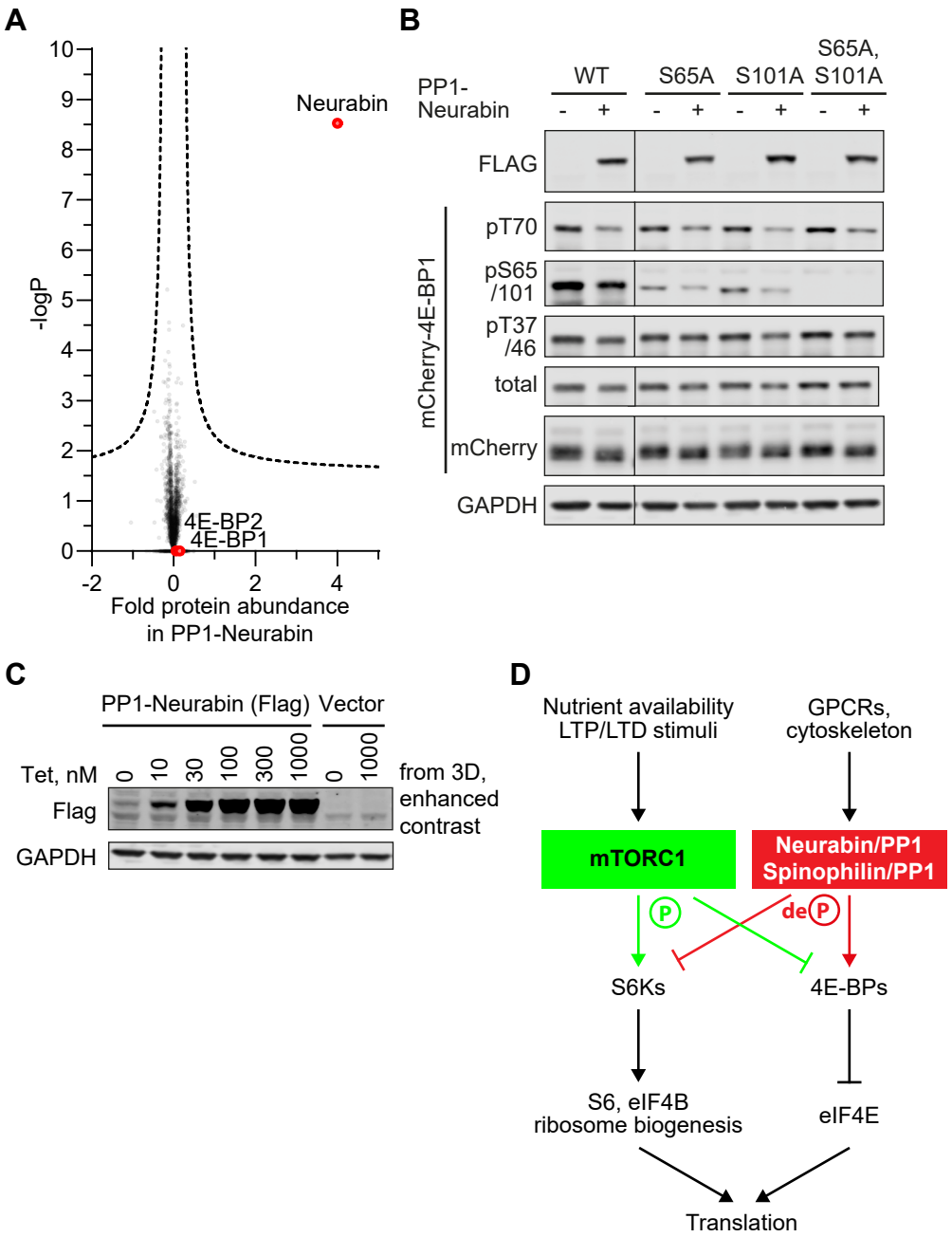
A
Neurabin
4E-BP2
4E-BP1
-logP
Fold protein abundance
in PP1-Neurabin
B
PP1-
Neurabin
WT
S65A
S101A
S65A,
S101A
FLAG
mCherry-4E-BP1
pT70
pS65
/101
pT37
/46
total
mCherry
GAPDH
C
PP1-Neurabin (Flag)
Vector
Tet, nM
Flag
GAPDH
from 3D,
enhanced
contrast
D
Nutrient availability
LTP/LTD stimuli
GPCRs,
cytoskeleton
mTORC1
Neurabin/PP1
Spinophilin/PP1
S6Ks
4E-BPs
S6, eIF4B
ribosome biogenesis
eIF4E
Translation

Figure 4

A

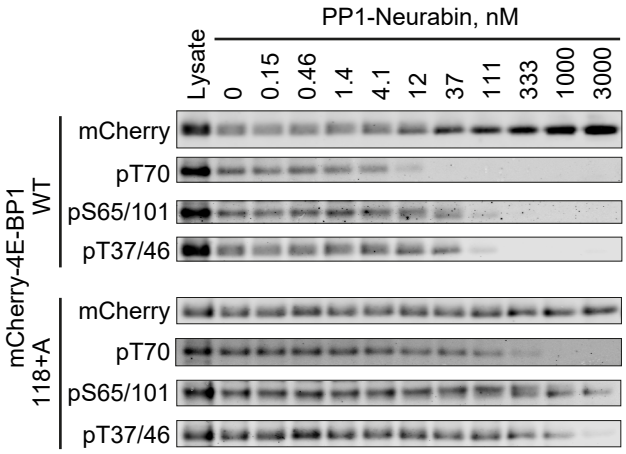

B

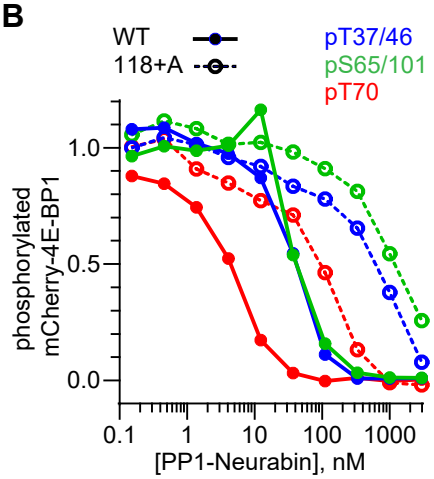

C

C-terminal peptides

		PDZ K_d, μM	
		Neurabin	Spinophilin
4E-BP1	EESQFEMDI	4.86 ± 0.15	23.4 ± 4.1
4E-BP1^{MUT}	EESQFESGS	nd	nd
S6K	RPEHLRMNL	147 ± 3	~480
Kalirin-7	PGDPFSTYV	179 ± 11	~280
GluR1	GMPLGATGL	>500	>500
GluR2	VYGIESVKI	>500	>500
GluN1-1	SDPSVSTVV	>500	>500
GluN2A	KMPSIESDV	>500	>500

D

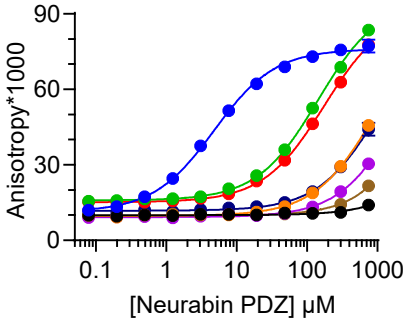

Figure 4-S1

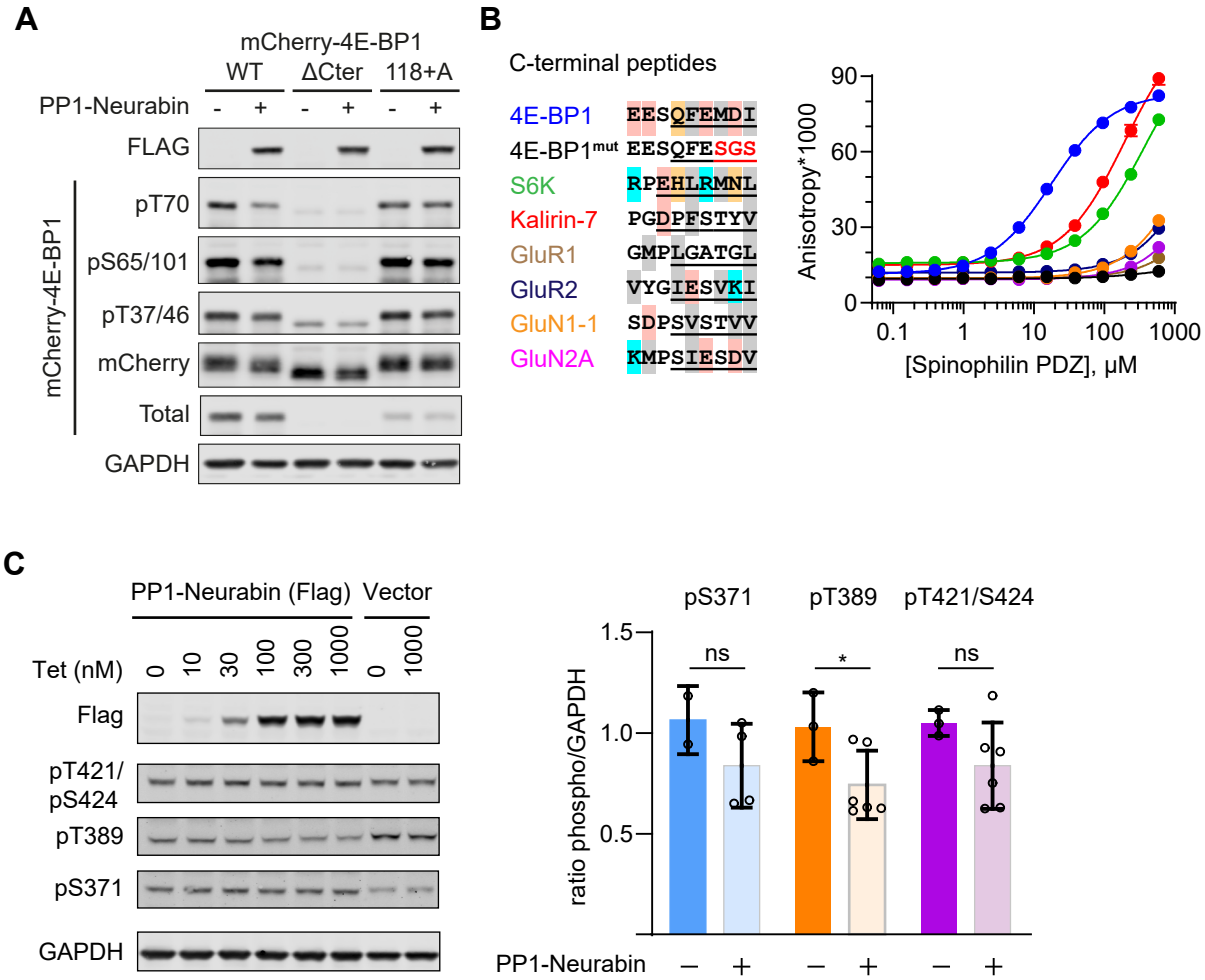
A
mCherry-4E-BP1
WT
ΔCter
118+A
PP1-Neurabin
- + - + - +
FLAG
pT70
pS65/101
pT37/46
mCherry
Total
GAPDH
mCherry-4E-BP1
B
C-terminal peptides
4E-BP1 EESQFEMDI
4E-BP1mut EESQFESGS
S6K RPEHLRMNL
Kalirin-7 PGDPFSTYV
GluR1 GMPLGATGL
GluR2 VYGIESVKI
GluN1-1 SDPSVSTVV
GluN2A KMPSIESDV
Anisotropy*1000
[Spinophilin PDZ], μM
C
PP1-Neurabin (Flag)
Vector
Tet (nM)
0 10 30 100 300 1000 0 1000
Flag
pT421/ pS424
pT389
pS371
GAPDH
pS371
pT389
pT421/S424
ratio phospho/GAPDH
ns
*
ns
PP1-Neurabin
– + – + – +

Figure 5

A

Substrate peptides

Neurabin/PP1 or Phactr1/PP1 dephosphorylation site — Neurabin PBM

		de-P site	+4/ +5/ +6	PDZ-binding	K_M, μM PP1-Neurabin	K_M, μM PP1-Phactr1
p4E-BP1^{PBM}	Ac-NSPVTK	(pT)	PPRDLPTI gsg	SQFEMDI	13.4 ± 4.2	-
p4E-BP1^{MUT}	Ac-NSPVTK	(pT)	PPRDLPTI gsg	SQFESGS	-	-
p4E-BP1$^{56A-PBM}$	Ac-NSPVTK	(pT)	PPRDAATI gsg	SQFEMDI	7.0 ± 5.6	-
p4E-BP1$^{34A-PBM}$	Ac-NSPVTK	(pT)	PPAALPTI gsg	SQFEMDI	7.4 ± 5.4	-
p4E-BP1$^{LLD-PBM}$	Ac-NSPVTK	(pT)	PPRLLDTI gsg	SQFEMDI	7.1 ± 6.0	-
p4E-BP1$^{12A-PBM}$	Ac-NSPVTK	(pT)	AARDLPTI gsg	SQFEMDI	11.1 ± 7.6	-
p4E-BP1^{2A-PBM}	Ac-NSPVTK	(pT)	PARDLPTI gsg	SQFEMDI	5.7 ± 3.0	-
p4E-BP1^{1A-PBM}	Ac-NSPVTK	(pT)	APRDLPTI gsg	SQFEMDI	14.3 ± 7.0	-
pIRSp53^{PBM}	Ac-QQGKSS	(pS)	TGNLLDKD gsg	SQFEMDI	10.8 ± 3.3	12.7 ± 8.0
pIRSp53^{MUT}	Ac-QQGKSS	(pS)	TGNLLDKD gsg	SQFESGS	-	14.5 ± 7.7
pIRSp53^{5A-PBM}	Ac-QQGKSS	(pS)	TGNLADKD gsg	SQFEMDI	8.8 ± 3.6	94 ± 31
pIRSp53^{5A-MUT}	Ac-QQGKSS	(pS)	TGNLADKD gsg	SQFESGS	-	108 ± 35

B

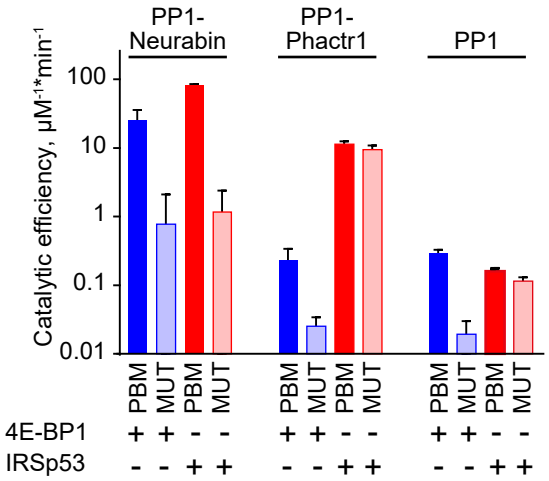

C

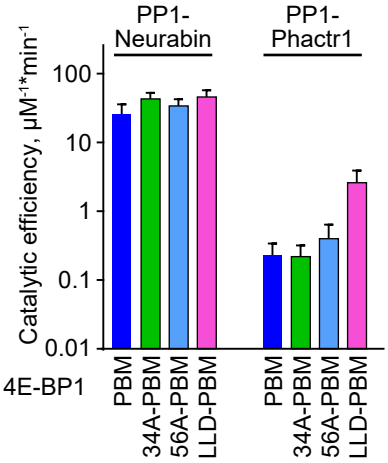

D

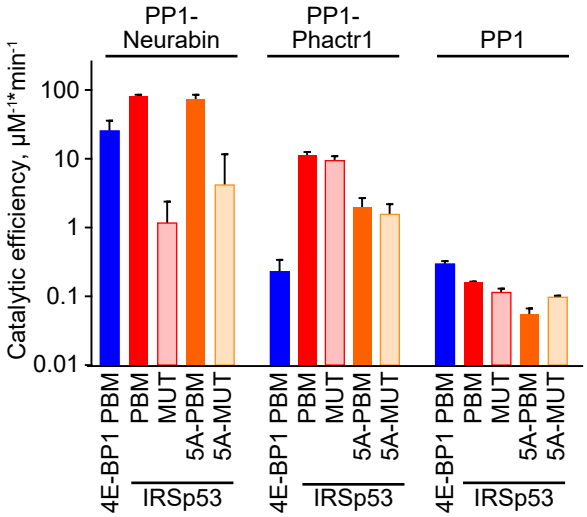

E

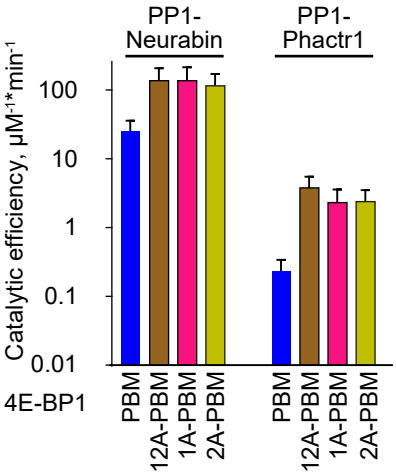

Figure 5-S1

A

	Catalytic efficiency, $\mu M^{-1}*min^{-1}$		
	PP1-Neurabin	PP1-Phactr1	PP1
p4E-BP1^{PBM}	25.3 ± 10.4	0.23 ± 0.11	0.30 ± 0.03
p4E-BP1^{MUT}	0.8 ± 1.3	0.026 ± 0.008	0.020 ± 0.010
p4E-BP1$^{56A-PBM}$	33.9 ± 8.7	0.40 ± 0.24	-
p4E-BP1$^{34A-PBM}$	43.1 ± 9.8	0.22 ± 0.10	-
p4E-BP1$^{LLD-PBM}$	45.7 ± 11.5	2.6 ± 1.3	-
p4E-BP1$^{12A-PBM}$	136.0 ± 71	3.8 ± 1.7	-
p4E-BP1^{1A-PBM}	137.0 ± 77	2.3 ± 1.3	-
p4E-BP1^{2A-PBM}	115.0 ± 57	2.4 ± 1.1	-
pIRSp53^{PBM}	81.9 ± 2.9	11.3 ± 1.2	0.160 ± 0.004
pIRSp53^{MUT}	1.2 ± 1.16	9.7 ± 1.2	0.12 ± 0.01
pIRSp53^{5A-PBM}	73.3 ± 11.8	2.0 ± 0.7	0.06 ± 0.01
pIRSp53^{5A-MUT}	4.3 ± 7.4	1.6 ± 0.6	0.100 ± 0.003

B

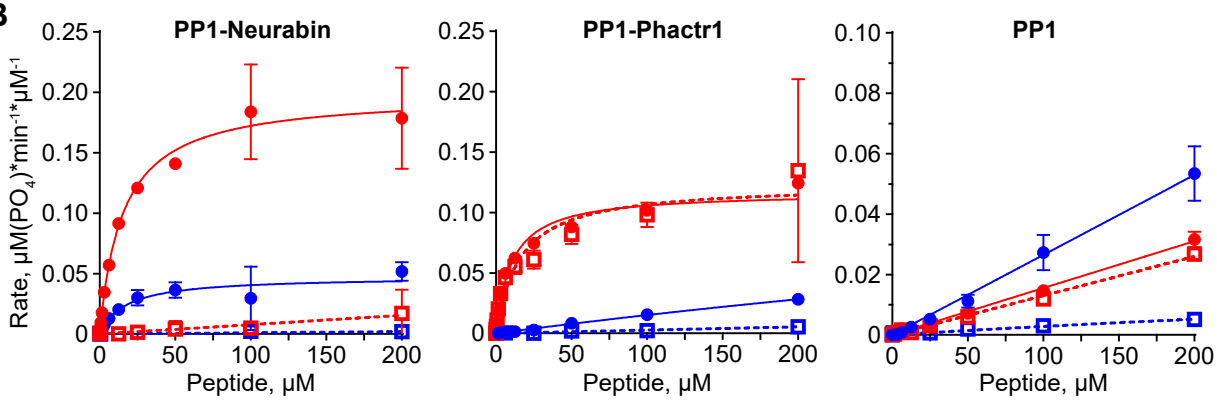

C

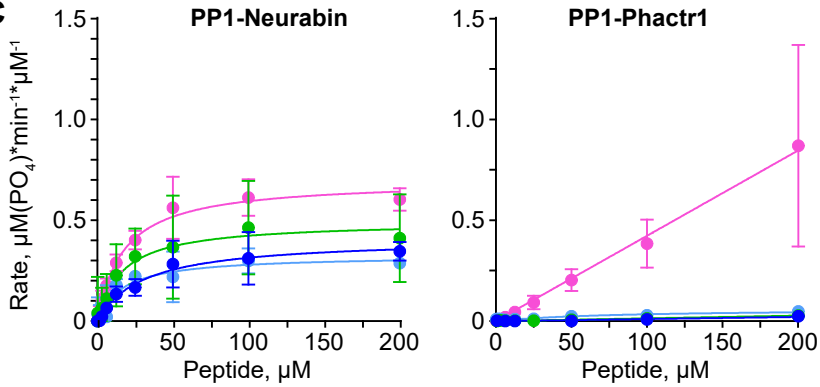

D

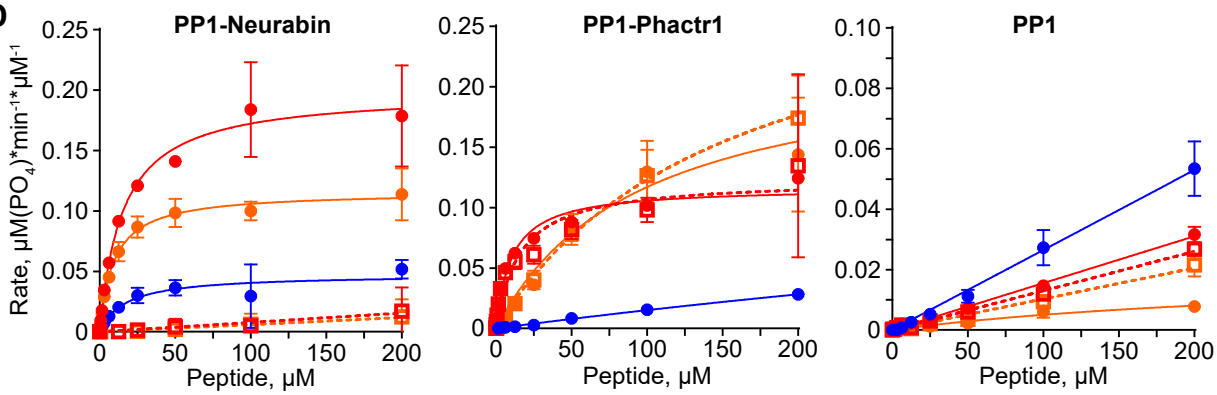

E

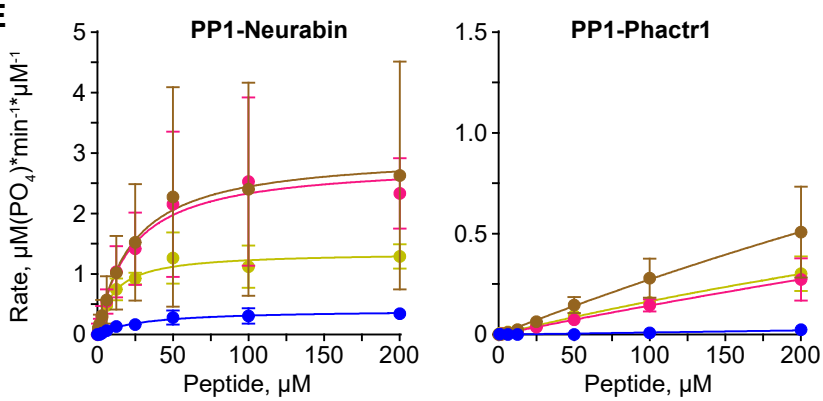

Figure 5-S2

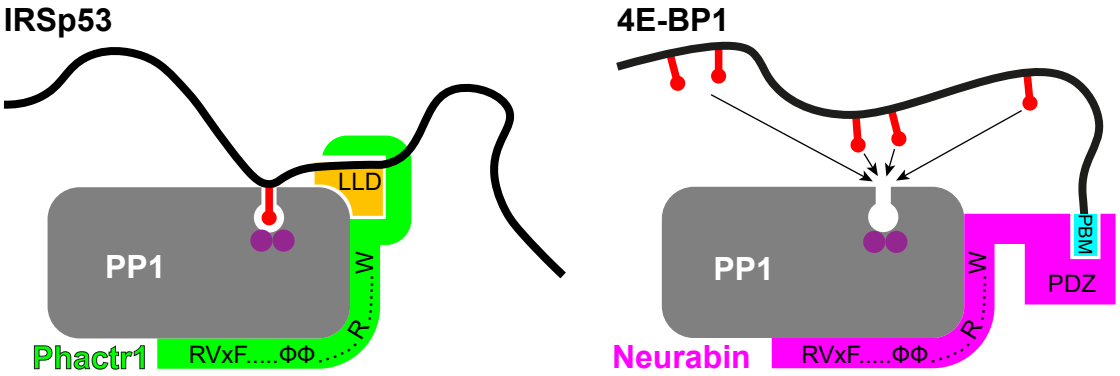
IRSp53
LLD
PP1
W
R
Phactr1
RVxF.....ΦΦ.....
4E-BP1
PP1
PBM
PDZ
W
R
Neurabin
RVxF.....ΦΦ.....

Figure 6

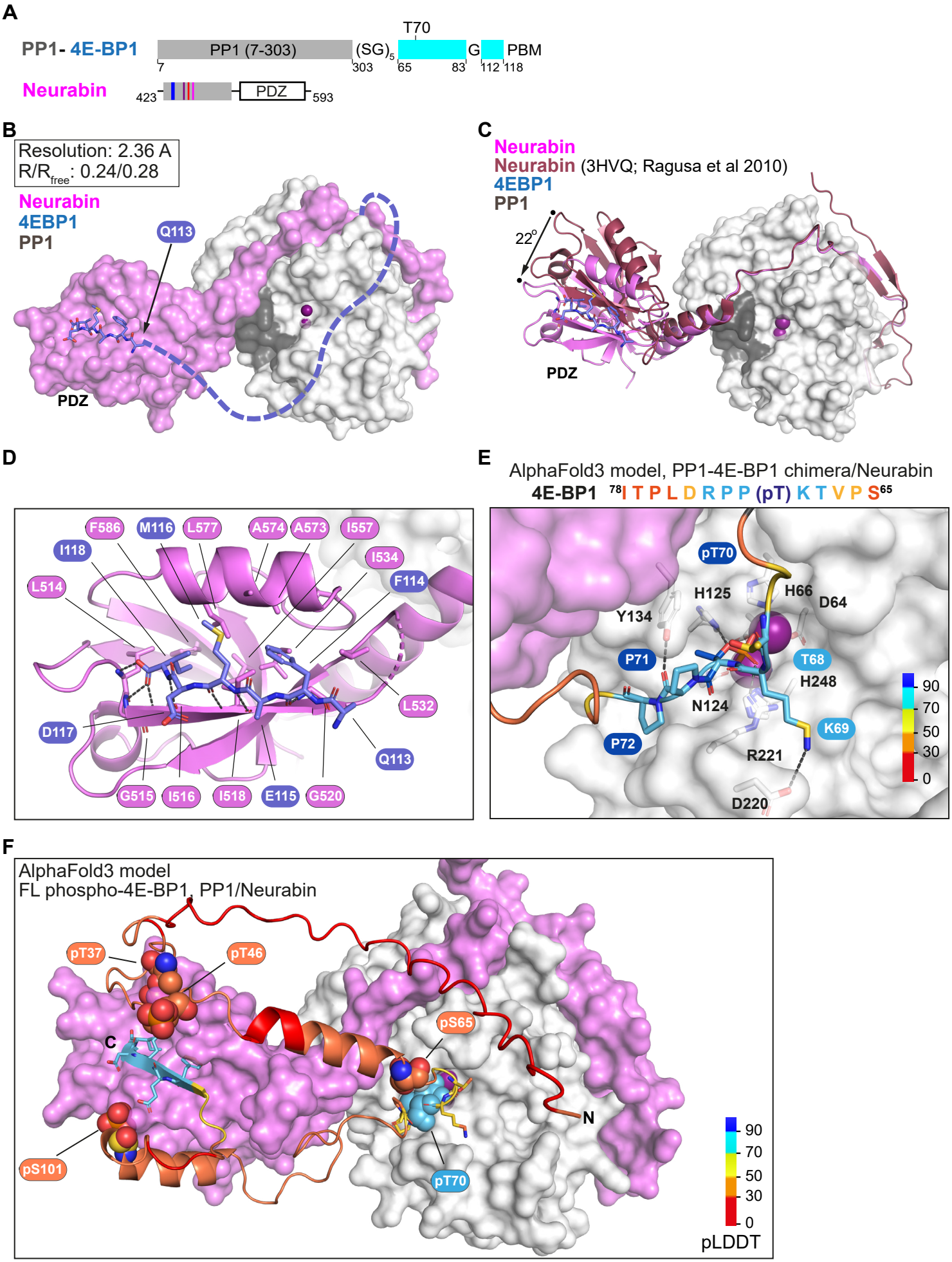
A
PP1- 4E-BP1
PP1 (7-303)
(SG)5
T70
G
PBM
7
303
65
83
112
118
Neurabin
423
PDZ
593
B
Resolution: 2.36 A
R/Rfree: 0.24/0.28
Neurabin
4EBP1
PP1
Q113
PDZ
C
Neurabin
Neurabin (3HVQ; Ragusa et al 2010)
4EBP1
PP1
22°
PDZ
D
F586
M116
L577
A574
A573
I557
I118
I534
L514
F114
L532
D117
Q113
G515
I516
I518
E115
G520
E
AlphaFold3 model, PP1-4E-BP1 chimera/Neurabin
4E-BP1 78I T P L D R P P (pT) K T V P S65
pT70
H125
H66
D64
Y134
P71
T68
H248
N124
K69
P72
R221
D220
90
70
50
30
0
F
AlphaFold3 model
FL phospho-4E-BP1, PP1/Neurabin
pT37
pT46
pS65
C
N
pS101
pT70
90
70
50
30
0
pLDDT

Figure 6-S2

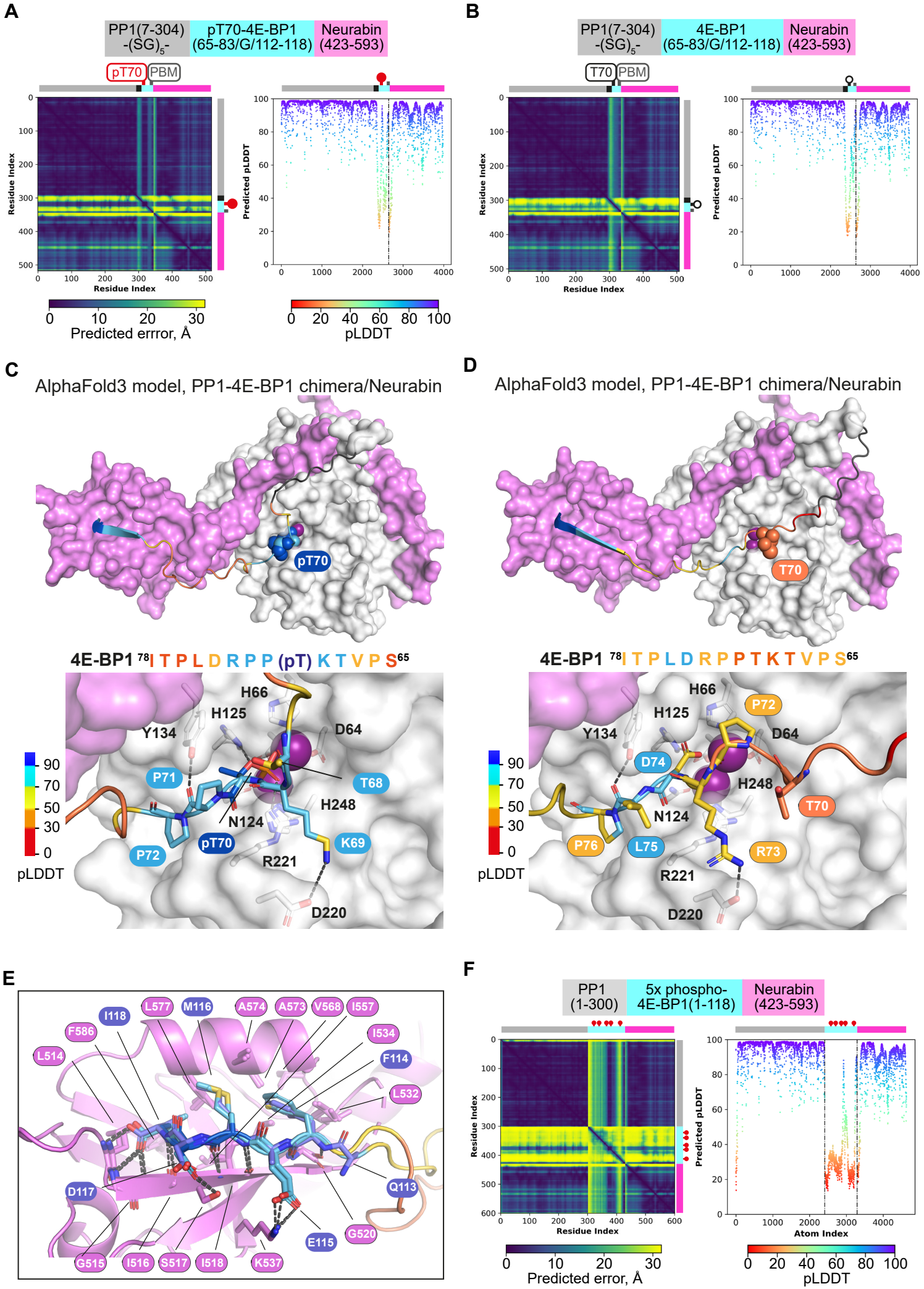
A
PP1(7-304) -(SG)5-
pT70-4E-BP1 (65-83/G/112-118)
Neurabin (423-593)
pT70
PBM
Residue Index
Predicted pLDDT
Predicted errror, Å
pLDDT
B
PP1(7-304) -(SG)5-
4E-BP1 (65-83/G/112-118)
Neurabin (423-593)
T70
PBM
C
AlphaFold3 model, PP1-4E-BP1 chimera/Neurabin
pT70
4E-BP1 78I T P L D R P P (pT) K T V P S65
H66
H125
Y134
D64
P71
T68
H248
N124
pT70
K69
P72
R221
D220
pLDDT
D
AlphaFold3 model, PP1-4E-BP1 chimera/Neurabin
T70
4E-BP1 78I T P L D R P P T K T V P S65
H66
P72
H125
Y134
D64
D74
H248
T70
N124
P76
L75
R73
R221
D220
pLDDT
E
I118
L577
M116
A574
A573
V568
I557
F586
I534
L514
F114
L532
D117
Q113
E115
G520
G515
I516
S517
I518
K537
F
PP1 (1-300)
5x phospho-4E-BP1(1-118)
Neurabin (423-593)
Residue Index
Predicted pLDDT
Atom Index
Predicted error, Å
pLDDT

Figure 6-S1

A

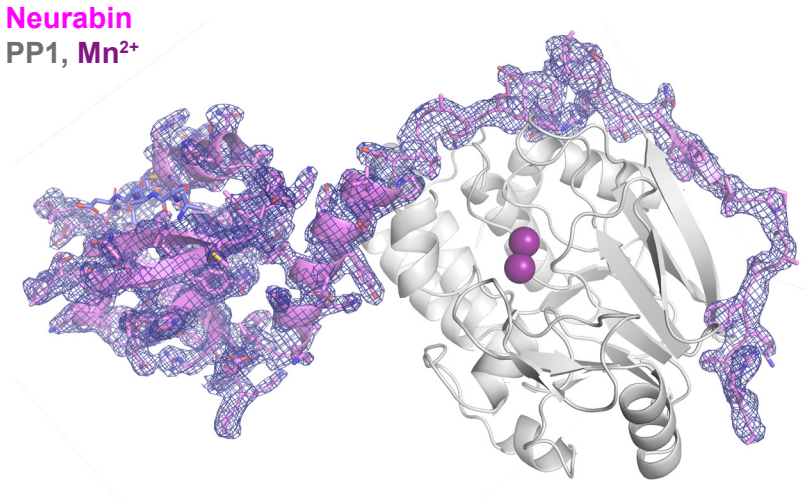

B

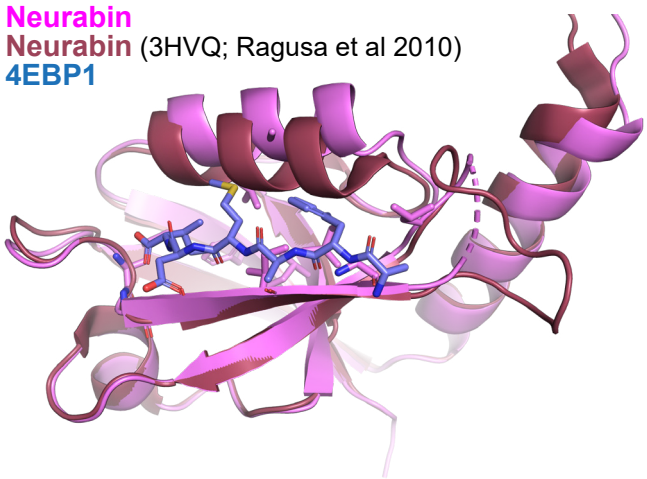

	(PDB accession number)
Resolution range	52.48 - 2.36 (2.42 - 2.36)
Space group	$C222_1$
Unit cell a, b, c	104.95 130.64 156.13
α, β, γ	90 90 90
Total reflections	1 207 183 (85 193)
Unique reflections	44 376 (3 023)
Multiplicity	27.2 (28.2)
Completeness (%)	98.91 (91.66)
Mean I/sigma(I)	5.29 (0.20)
Wilson B-factor	49.25
R-merge	0.31 (12.11)
R-meas	0.32 (12.33)
R-pim	0.06 (2.30)
CC1/2	0.99 (0.28)
Reflections used in refinement	44 019 (2 889)
Reflections used for R-free	1 996 (131)
R_{work}	0.24 (0.36)
R_{free}	0.28 (0.32)
Number of non-hydrogen atoms	6 180
macromolecules	6 156
ligands	4
solvent	20
Protein residues	787
RMS(bonds)	0.003
RMS(angles)	0.61
Ramachandran favoured (%)	95.74
Ramachandran allowed (%)	4.26
Ramachandran outliers (%)	0.00
Clash score	3.23
Average B-factor	57.04
macromolecules	57.05
ligands	68.46
solvent	50.83

Table1: Crystallographic data and refinement statistics.